TITLE: Organellular imaging *in vivo* reveals a depletion of endoplasmic reticular calcium during post-ictal cortical spreading depolarization

AUTHORS: Matthew A. Stern[1], Eric R. Cole[1,2], Claire-Anne Gutekunst[1], Jenny J. Yang[3], Ken Berglund[1*] and Robert E. Gross[1†]

AFFILIATIONS:
[1]Department of Neurosurgery, Emory University School of Medicine, Atlanta, GA, United States
[2]Coulter Department of Biomedical Engineering, Emory University and Georgia Institute of Technology, Atlanta, GA, United States
[3]Department of Chemistry, Center for Diagnostics and Therapeutics, Advanced Translational Imaging Facility, Georgia State University, Atlanta, GA, United States
*Corresponding author: Ken Berglund, ken.berglund@emory.edu
†Present Address: Department of Neurological Surgery, Rutgers Robert Wood Johnson Medical School, New Brunswick, NJ, United States

ABSTRACT

During cortical spreading depolarization (CSD), neurons exhibit a dramatic increase in cytosolic calcium, which may be integral to CSD-mediated seizure termination. This calcium increase greatly exceeds that during seizures, suggesting the calcium source may not be solely extracellular. Thus, we sought to determine if the endoplasmic reticulum (ER), the largest intracellular calcium store, is involved. We developed a two-photon calcium imaging paradigm to simultaneously record the cytosol and ER during seizures in awake mice. Paired with direct current recording, we reveal that CSD can manifest as a slow post-ictal cytosolic calcium wave with a concomitant depletion of ER calcium that is spatiotemporally consistent with a calcium-induced calcium release. Importantly, we observed both naturally occurring and electrically induced CSD suppressed post-ictal epileptiform activity. Collectively, this work links ER dynamics to CSD, which serves as an innate process for seizure suppression and a potential mechanism underlying therapeutic electrical stimulation for epilepsy.

MAIN TEXT

INTRODUCTION

The endoplasmic reticulum (ER), a major calcium reservoir of the cell, is critically involved in essential physiological processes. The perturbation of ER homeostatic regulation in turn has serious pathophysiologic implications[1]. This is especially the case for the nervous system, where intra- and inter-cellular communication is tightly regulated through the ER calcium, including synaptic transmission, transcriptional regulation and plasticity[2-4]. Deciphering calcium signaling dynamics at a spatiotemporal level during aberrant activity could inform our understanding of disease mechanisms and their downstream sequelae. Calcium imaging of the ER has been enabled through the development of various ER targeted dyes and genetically encoded calcium indicators[5, 6], but these have hitherto not been applied *in vivo* to vertebrates. Thus, we devised an approach for concurrent *in vivo* calcium imaging of the cytosol and ER. We then applied this approach to elucidate the difference between two related neurological phenomena both causing high intracellular calcium: seizures and cortical spreading depolarization (CSD)[7].

CSD was first documented in 1944, when Aristides Leão reported his first series of electrocorticography recordings of slow propagating waves of depression in rabbit cortex, an investigation he began originally to induce epileptiform discharges[8, 9]. He would later go on to characterize these traveling waves as large scale depolarizing events, exhausting the tissue into a state of depression, hence the term CSD[10]. While CSD is largely considered to be pathologic across a wide array of diseases[11-15], its relationship with seizures appears to be more complicated [16]. Observations in animal models[17-20] and patients[21, 22] have demonstrated a strong association between the two events with CSD occurring often at the end of seizures. Indeed, the ionic shifts that occur during seizures are conditions that parallel those of CSD. Large extracellular deposition of glutamate and potassium[7, 23] and the shrinking of extracellular space[24, 25] create a hyperexcitable state for neurons that can beget CSD, in a feedforward amplificatory fashion[26]. The subsequent impact of CSD in seizures is both deleterious and protective, being implicated as an underlying cause of sudden unexplained death in epilepsy (SUDEP)[27], as well as a mechanism of seizure termination[17]. Thus, having a better understanding of the interplay between these two neurologic phenomena could be of vital importance for both the suppression of seizures, as well as prevention of one of epilepsy's most feared complications.

In our previous studies using *in vivo* two-photon calcium imaging in awake mice to evaluate seizure dynamics[28], we observed slow propagating calcium waves at the end of seizures, which corresponded with an absence of high frequency neuronal firing in electrocorticography (EEG). We hypothesized that these may be CSD, as large calcium transients are a known occurrence during spreading depolarizations[29, 30] and have been observed as waves[31] with similar spatiotemporal properties. As the increase in intracellular calcium during CSD exceeds that during seizures[7], extracellular influx is unlikely to be the only contributing source of calcium, raising the possibility of ER involvement. Furthermore, since elevated calcium levels are hypothesized to mediate seizure termination[32], this dramatic calcium rise may underly the purported seizure suppressive effects of CSD.

To investigate the mechanisms underlying these stark intracellular increases in calcium, we generated an adeno-associated viral (AAV) vector to transduce neurons with two calcium indicators at the same time, each targeted to a separate intracellular compartment. In the cytosol we express a yellow derivative of the GCaMP family, XCaMP-Y[33], and in the ER lumen we express a red indicator, RCatchER[34]. RCatchER is a low affinity ($K_d = \sim 400\ \mu M$) calcium indicator protein with fast kinetics (<1 ms) and a fluorescence intensity that varies linearly with calcium concentration, making it an optimal indicator for ER calcium. We then intravitally recorded generalized seizures[35] in awake mice, concurrently with EEG and direct current (DC) recordings, with DC being the gold standard for confirmation of CSD.

In the present study we determine that these slow propagating post-ictal calcium waves are in fact CSDs. We next show that CSD is marked by a stark depletion of ER calcium not occurring during normal or epileptiform activity. Our spatiotemporal analysis at a cellular level indicates that this depletion is consistent with a calcium-induced calcium release (CICR). In addition, we observe that depletion of ER calcium also occurs during CSD evoked by electrical stimulation. Finally, we provide causal evidence that naturally occurring CSD is associated with a suppression of post-ictal epileptiform activity and this same suppression can be achieved through the biologically similar electrically evoked CSD. Collectively this work offers new insight into the biological underpinnings of CSD and its potential utility for seizure control.

RESULTS

93

Intravital imaging of cytosol and ER calcium stores in awake mice

94

95 To study intracellular calcium dynamics *in vivo* with high spatiotemporal resolution, we developed

96 a recombinant AAV to express two genetically encoded calcium indicators (GECIs) of different

97 colors pan-neuronally through the human synapsin I (hSynI) promoter[36]. The yellow XCaMP-Y[33]

98 and the red-shifted RCatchER[34] GECIs were separated by the self-cleaving P2A peptide to obtain

99 similar expression levels (Fig. 1a). While the XCaMP-Y will be localized to the cytosol, the

100 RCatchER includes calreticulin and KDEL sequences, for targeting and retention in the ER lumen,

101 respectively. We confirmed this expression pattern by immunohistochemistry (Fig. 1b). These

102 indicators were selected for their ability to be simultaneously excited with a single wavelength of

103 light between 1000 and 1040 nm (Fig. 1c). Emission was bandpass filtered to isolate each's distinct

104 signal, thus enabling simultaneous calcium imaging in the two subcellular compartments with

105 single cell resolution. We stereotaxically injected this AAV into the motor cortex of mice and

106 installed chronic cranial windows with head plates to facilitate repeated imaging within subjects.

107 We then performed awake, head-fixed imaging in cortical layers 2/3 (Fig. 1d) to record cytosolic

108 and ER calcium changes across hundreds of neurons in the field (Fig. 1e). During spontaneous

109 locomotion activity, we observed transient increases in cytosolic calcium, classically serving as a

110 proxy for neuronal activity/action potentials, while the ER calcium remained relatively stable (Fig.

111 1f-i) in contrast to the subsequent recordings during pathologic activity.

112
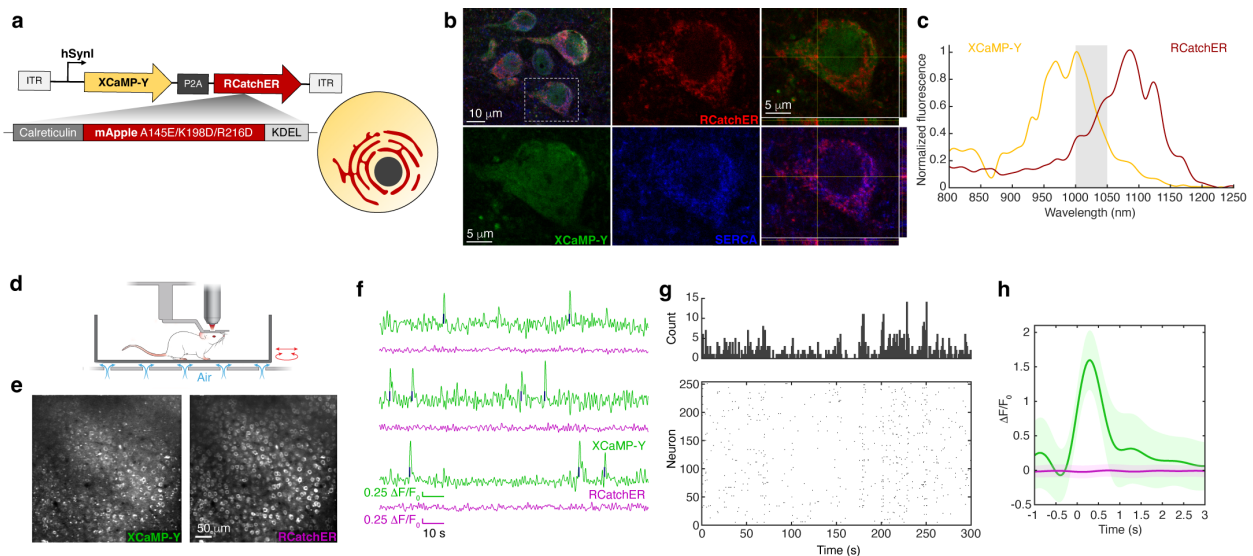
113
114

Figure 1. Dual-color two-photon simultaneous intravital calcium imaging of the cytosol and ER during neuronal activity in awake mice

115
116

117 **(a)** Schematic of AAV cassette encoding the XCaMP-Y and RCatchER GECIs (left) enabling

118 mutually exclusive expression in cytosol and ER respectively (right). **(b)** Immunohistochemistry

119 (confocal) demonstrating localization of XCaMP-Y and RCatchER to the cytosol and ER

120 respectively, with RCatchER but not XCaMP-Y colocalized with the ER marker SERCA.

121 Reconstructions of Z axis at crosshairs presented (right). **(c)** Overlapping two-photon excitation

122 spectra of the XCaMP-Y and RCatchER captured *in vivo* (N=1 mouse; n=298 neurons) with the

123 wavelengths used for simultaneous activation highlighted in grey. **(d)** Illustration of awake *in vivo*

124 recording set-up of a head-fixed-mouse poised on air-suspended chamber. **(e)** Representative field

3

125 of view (cortical layer 2/3; depth: 200 mm from pial surface) showing time-averaged projections
126 of cells expressing both XCaMP-Y (left, green channel) and RCatchER (right, red channel). **(f)**
127 Representative individual cell normalized calcium fluorescence traces ($\Delta F/F_0$) of XCaMP-Y
128 (green) and RCatchER (magenta), with detected spike times indicated (blue). **(g)** Spike raster and
129 corresponding histogram (1s bin width) of spontaneous firing detected in XCaMP-Y during 5 min
130 of baseline recording (N=1 subject; n=254 neurons). **(h)** Average spike trace relative to indexed
131 spike time, presented with pooled standard deviation of signal (shaded area).
132
133 **CSD observed at generalized seizure termination is marked by a unique depletion of ER**
134 **calcium**
135 For recording the calcium dynamics during seizures and purported CSD, we coupled our dual-
136 color two-photon imaging with simultaneous EEG and DC recording (Fig. 2a). We recorded EEG
137 through chronically implanted electrodes and DC through a glass microelectrode attached to a DC
138 amplifier. To enable this, we fabricated multipaned concentric glass windows with silicone access
139 ports for repeated access to the brain (Fig. 2a and Supplementary Fig. 1). We induced epileptiform
140 activity by subcutaneous administration of pentylenetetrazol (PTZ; s.c. 40-50 mg/kg; N=9
141 subjects, 30 recordings; Fig. 2a-c). We recorded 23 generalized seizures (Fig. 2b), 4 of which were
142 fatal (analyzed separately in a subsequent section). For the non-fatal seizures, we observed pre-
143 ictal spikes (PIS) across all three recording modalities (Fig. 2d, e), beginning within a few minutes
144 of PTZ injection (234±29 s (mean ± SE); N=19 seizures, 8 subjects). Typically, within 10 minutes
145 (471±53 s), we observed a seizure (length: 21±3 s) on EEG followed by a quiescent post-ictal
146 period. Concurrent calcium transients were observed through the cytosolic calcium indicator,
147 while ER calcium stayed relatively stable. Soon after termination of a seizure, we sometimes
148 observed a large and sustained increase in cytosolic calcium (23±5 s; N=6 seizures, 5 subjects),
149 concomitant with a negative DC shift, a hallmark of CSD (17.03±2.85 mV; N=4 seizures, 4
150 subjects with DC recording). This calcium change was comparable to that observed during seizures
151 (p=0.688, generalized linear mixed effects model (GLME), N=6 seizures, 5 subjects, 116-371
152 cells/recording), and greater than that occurring during PIS (p=2.87×10^{-21}). We also observed a
153 concurrent large, rapid and sustained depletion of ER calcium which was significantly larger than
154 calcium changes occurring during the seizure or PIS (p=1.88×10^{-10} (CSD to seizure), p=7.01×10^{-17}
155 (CSD to PIS); Fig. 2c-e and Supplementary Fig. 2). PTZ administration did not always induce
156 seizures and CSD (Fig. 2b): it could also induce seizures without CSD, or epileptiform spiking
157 (spike-wave discharges, SWDs) that did not progress to seizure (sub-generalized). We did not
158 observe a comparable change in ER calcium during these events. The large increase in cytosolic
159 calcium and ER depletion was specific to CSD and not a general post-ictal phenomenon, with
160 statistically larger changes in post-ictal calcium during CSD as compared to the same post-ictal
161 period in those seizures without CSD (p= 0.0273 (cytosol), p=9.21×10^{-21} (ER), GLME, N=17
162 seizures (11 without, 6 with CSD), 8 subjects, 43-371 cells/recording; Fig. 2f). Taken together, we
163 confirmed that the slow propagating cytosolic calcium waves observed at the end of seizures
164 corresponded to CSD with the iconic DC shifts, and a depletion of ER calcium stores.
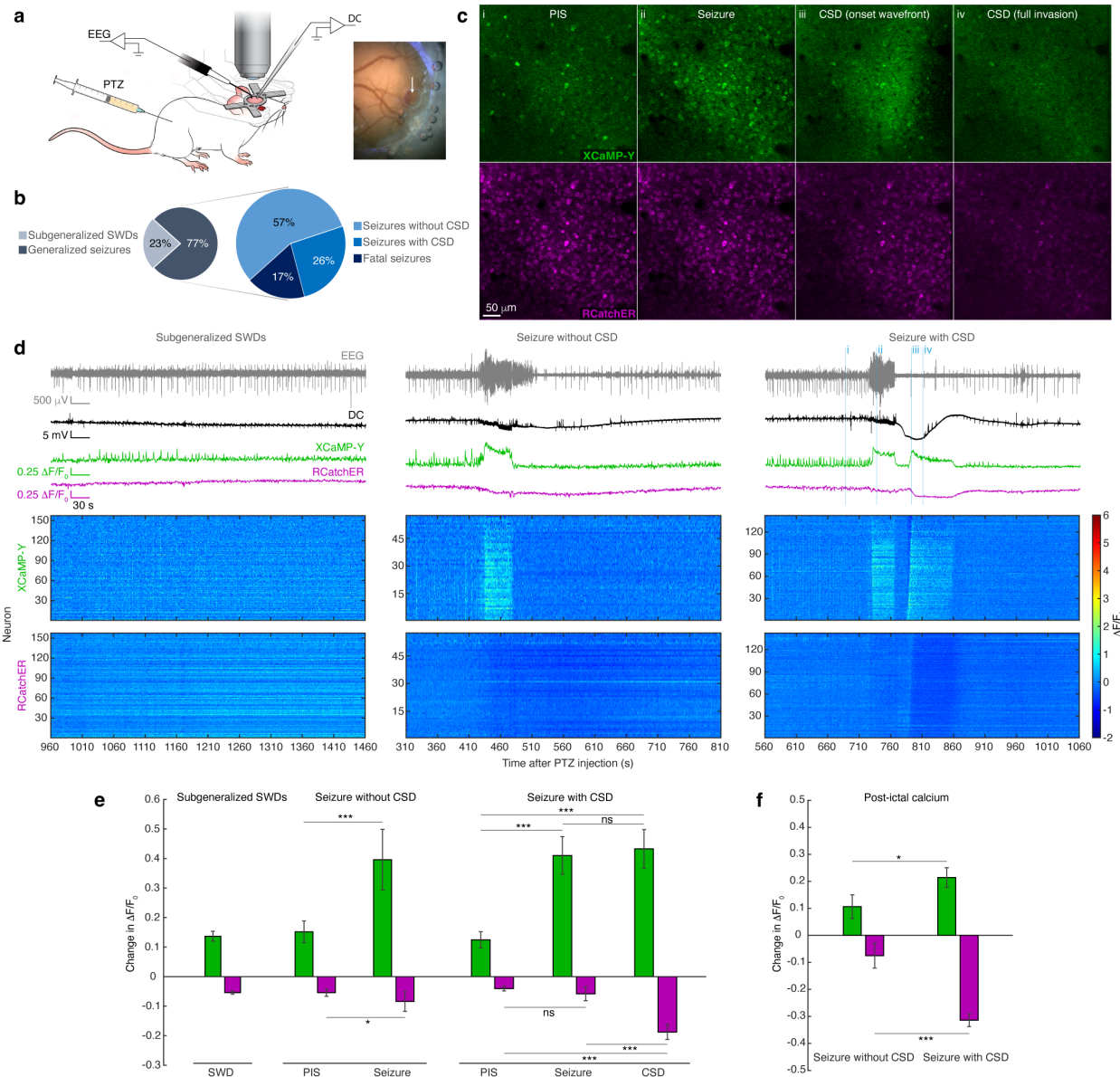165

4

Figure 2. CSD is associated with generalized seizure termination and is marked by a unique depletion of ER calcium stores

(a) Illustration depicting the awake head fixed two-photon imaging along with simultaneous EEG and DC recording during PTZ-induced seizures (left). Image of cranial window with glass electrode inserted through silicone access port (white arrow, right). **(b)** Pie charts representing proportion of PTZ injections (N=30) that resulted in generalized seizures (N=23) (left) and, of those generalized seizures, the proportions that occurred with (N=6) or without CSD (N=13) or that were fatal (N=4) (right). **(c)** Representative frames by channel during a PTZ-induced generalized seizure recording depicting the cytosolic (top row) and ER (bottom row) calcium changes during a PIS (i), the seizure (ii) and the CSD (iii: wavefront invasion, iv: CSD after full invasion). Note depletion (left side) of calcium in the recruited area during CSD invasion. **(d)** Mean population calcium fluorescence (XCaMP-Y: green, RCatchER: magenta) with synchronized EEG (grey) and DC (black) recordings during three separate recording sessions

5

181   within the same subject depicting sub-generalized epileptiform activity and seizures with and
182   without CSD. Corresponding rasters of individual cell calcium transients are presented below (y-
183   axis: neurons ordered from left to right across the field). **(e)** Group level analysis of the average
184   individual cell changes in calcium during each event phase (PIS, seizure and CSD) across each
185   recording type (sub-generalized: N=4 subjects, 7 recordings; seizure without CSD: N=6 subjects,
186   12 recordings; and seizure with CSD: N=5 subjects, 6 recordings; n=43-413 cells per recording).
187   **(f)** Average post-ictal calcium changes are presented for the seizure recordings with and without
188   CSD. N=17 seizures (11 without, 6 with CSD), 8 subjects, 43-371 cells/recording. The effect of
189   event on calcium levels are modeled using GLME for e and f. Means with pooled standard error
190   are presented in all bar plots. *p<0.05, **p<0.01, ***p<0.001.

191

192   **ER calcium depletion during seizure CSD is consistent with a CICR**
193   Having established the sustained post-ictal calcium depletion in the ER to be specific to CSD, we
194   next sought to characterize the spatiotemporal features of these changes. Both cytosolic and ER
195   calcium changes appeared as a wavefront of propagation (Fig. 3a; Supplementary Movie 1). To
196   determine the timing of the changes across the individual cells, we leveraged our slope integral
197   feature detection approach for seizure traveling waves[28] to find the times individual cells were
198   recruited to the CSD in XCaMP-Y and the time of their ER depletion in RCatchER (Fig. 3b). We
199   generated a colormap depicting relative recruitment times within the channels in the field of view
200   (Fig. 3c). Wavefronts in both channels appeared to move in the same direction, with the wave in
201   the ER slightly delayed.
202   We performed a spatial linear regression[37, 38] on the recruitment times to determine the
203   wavefront vectors of propagation. We present this first as a polar plot, where the arrows illustrate
204   the direction and speed of the regressed vector of propagation, indicating the overlap in vectors
205   between channels (Fig. 3d and Supplementary Fig. 3). We found that the cytosolic increase and
206   ER depletion propagated in a contiguous fashion, with comparable velocities to each other (Fig.
207   3d-f). These velocities are consistent with typical CSD velocity[7, 31]. We observed that both
208   cytosolic and ER calcium changes were delayed relative to the CSD DC shift onset (cytosolic:
209   11.35±0.35 s; ER: 11.77±0.50 s; mean ± SE; N=4 seizures, 4 subjects, 142-371 cells/recording).
210   This is concordant with the DC recording site being about 1 mm lateral to the field of view and
211   thus earlier in the wavefronts' paths of propagation medially, given the determined velocities of
212   propagation. We next plotted the recruitment times within each channel relative to their projected
213   position along the determined axis of propagation in the cytosolic channel (Fig. 3g). This analysis
214   demonstrated a consistently delayed ER depletion along the same axis of propagation as the
215   cytosolic increase. ER depletion was also found to follow the cytosolic increase within each cell
216   (Fig. 3h), with a significant delay of about 1 second (0.79±0.42 s, p=3.37×10⁻⁸, GLME, N=6
217   seizures, 5 subjects, 116-371 cells/recording).
218   Interestingly, the loss of calcium from the cytosol and return of calcium to the ER also
219   followed a wavefront pattern, occurring in roughly the same direction as the invasion, although
220   with a slower speed (Fig. 3b-g, i; offset). Unlike the initial change in calcium during the CSD
221   invasion, this subsequent change at the end of CSD was more gradual, making the slope integral
222   feature and maximum slope more difficult to discern at the individual cell level. Therefore, we
223   chose to use the point of maximal concavity, the elbow, being the point when a change started. We
224   again found a delay in recruitment relative to the DC shift, consistent with the slower propagation
225   speed of this change (cytosolic: 24.55±0.90 s; ER: 28.15±1.21 s). Computing the time delay
226   between these onsets and offset events within cells, we found lengths of change of calcium

227 comparable between the cytosol and ER (Fig. 3j) and consistent with the average duration of the
228 DC shift (38.93±4.88 s, N=4 seizures, 4 subjects). This short delay in ER calcium release following
229 the same spatiotemporal pattern at the cytosolic increase during CSD, with comparable velocity
230 and duration, suggests a CICR is occurring.
231
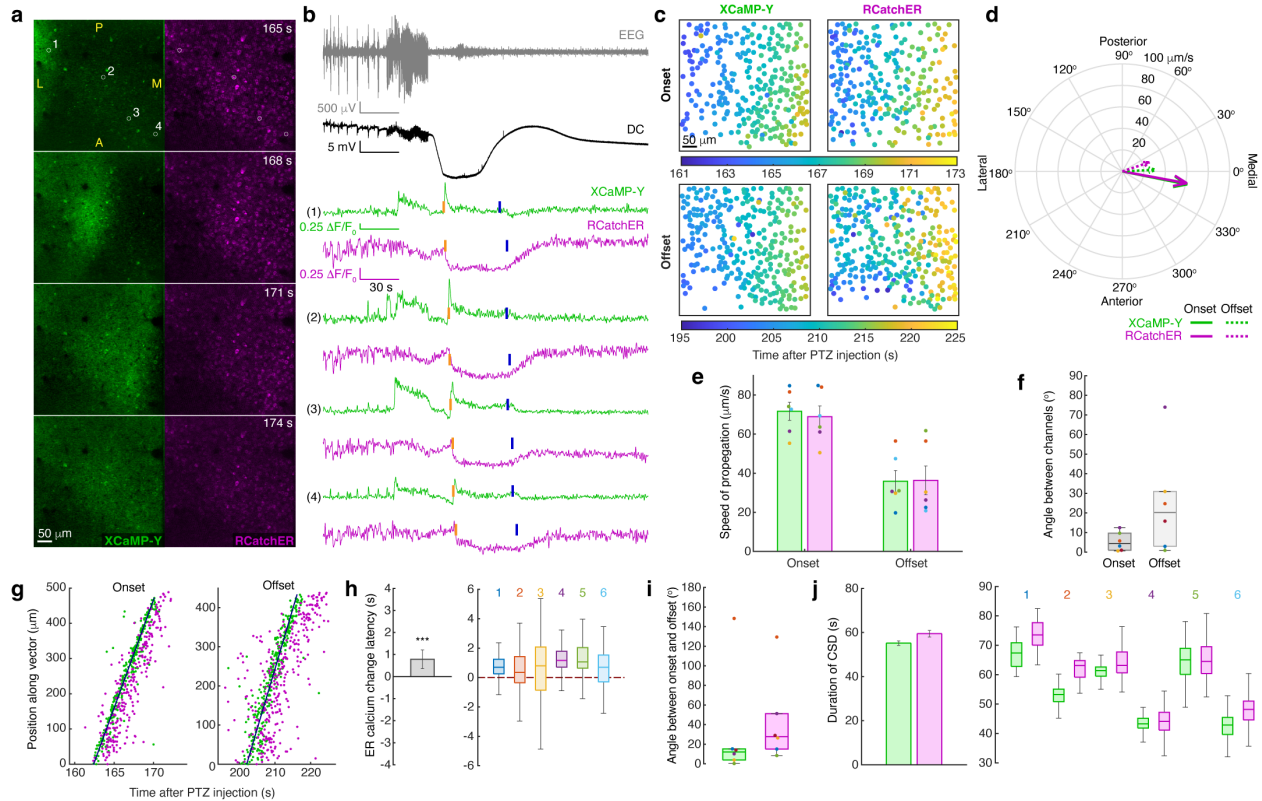
234 **Figure 3. Spatiotemporal dynamics of subcellular compartment calcium changes during**
235 **CSD**
236 **(a)** Time lapse images depicting the represented CSD wavefront invasion calcium changes. Circles
237 indicate regions of interest (ROIs) of the representative traces in b. Field orientation is indicated
238 (A: anterior, L: lateral, M: medial, P: posterior). **(b)** Representative individual cell calcium traces
239 of XCaMP-Y (green) and RCatchER (magenta), during generalized seizures occurring with post-
240 ictal CSD along with concurrent EEG (grey) and DC (black) traces. The detected recruitment times
241 to the CSD invasion wavefront are indicated in orange and subsequent calcium changes at the
242 offset of the CSD in blue. **(c)** ROI colormap of determined recruitment times for identified cells
243 during the onset and offset of the representative CSD in panel a, with color corresponding to
244 recruitment time. **(d)** Polar plot of the CSD onset and offset propagation vectors modeled by
245 applying spatial linear regression to the neuronal recruitment times shown in panel c, showing
246 wavefront direction (vector angle) and propagation speed (vector magnitude). **(e)** Average speed
247 of CSD propagation at the onset and offset of the event by channel with standard error. Each CSD
248 is depicted using a unique color matched across all the panels in this figure. **(f)** Absolute difference
249 in direction between the XCaMP-Y and RCatchER vectors at the onset and offset of CSD. **(g)**
250 Individual cell recruitment times by channel of the CSD onset and offset projected on to the
251 propagation axis of XCaMP-Y. **(h)** Mean ER calcium change latency relative to the cytosolic
252 calcium change within cell during CSD invasion across all recordings with pooled standard error

253   (left) and the distribution of these latencies for each recording (right). The effect of channel on
254   recruitment times used to compute these latencies are modeled using GLME. **(i)** Absolute
255   difference in direction between the onset and offset vectors of the CSD within channel. **(j)** Average
256   duration of CSD within cell by channel across recordings with pooled standard error (left) and the
257   distribution of the event durations for each recording (right). For group level analysis (e, g, h-j)
258   N=6 seizures across 5 subjects with n=116-371 cells per recording. *p<0.05, **p<0.01,
259   ***p<0.001.
260

261   Occasionally the seizure induced was fatal for the subject (Fig. 2b). For these, a terminal spreading
262   depolarization (TSD) was observed following the seizure during isoelectric EEG, with a negative
263   DC shift (-8.84±0.67 s; mean ± SE; N=4 seizures, 4 subjects) that did not recover (Fig. 4a).
264   Additionally, the initial spatiotemporal changes in calcium observed upon TSD invasion were
265   similar to those observed with CSD in the non-fatal seizures. The waves propagated with similar
266   speeds and direction (Fig. 4b-e), with the depletion of ER calcium following the cytosolic increase,
267   albeit with a slightly longer delay (Fig. 4f, g), and smaller magnitude of cytosolic calcium change
268   (Fig. 4h). Notably, the calcium changes did not return to their baseline values, with cytosolic
269   calcium remaining high and ER depleted, consistent with cell death.
270
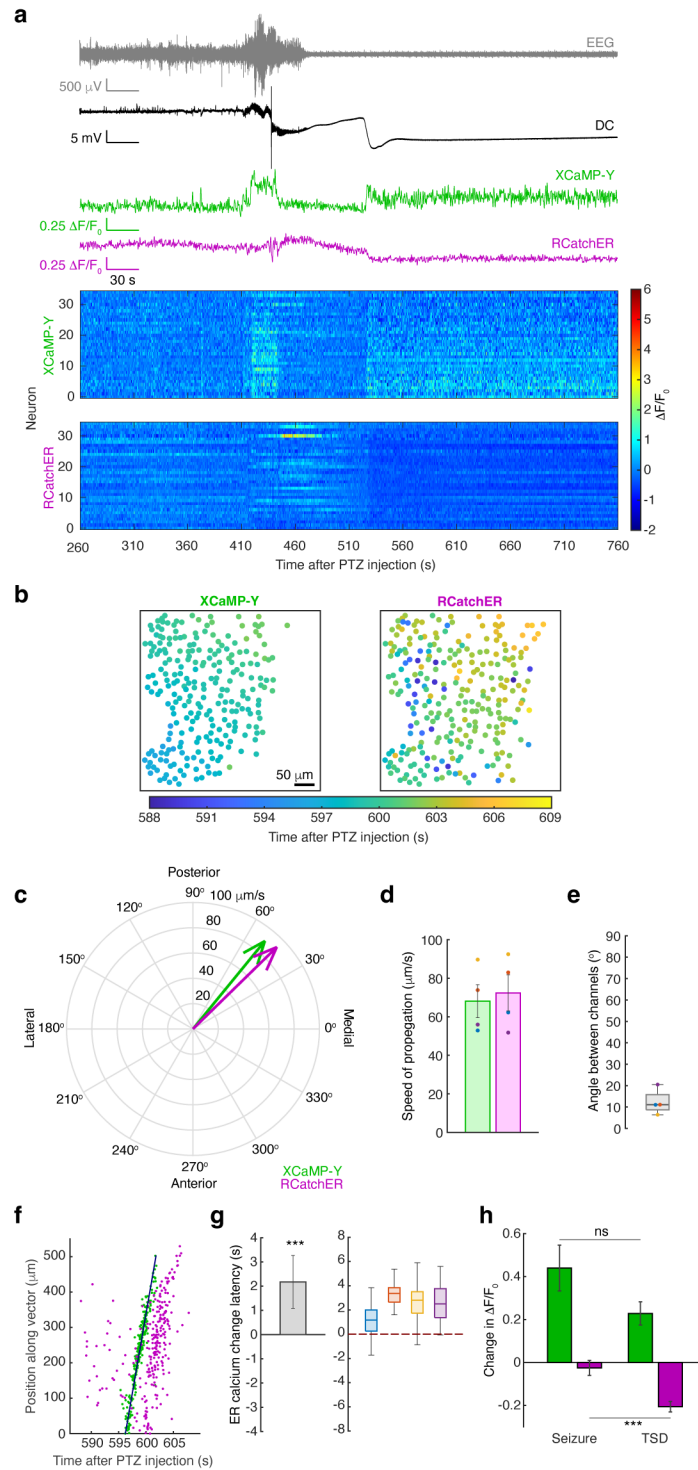
Figure 4. TSD observed during fatal seizures demonstrate a permanent increase in cytosolic calcium and depletion of ER calcium stores.

(a) Mean population calcium fluorescence (XCaMP-Y: green, RCatchER: magenta) with synchronized EEG (grey) and DC (black) recordings during a fatal generalized seizure occurring with TSD from a representative subject. Corresponding rasters of individual cell calcium transients (y-axis: neurons ordered from left to right across the field) are presented below. **(b)** ROI colormap

9

279 of determined recruitment times for identified cells during TSD, with color corresponding to
280 recruitment time. **(c)** Polar plot of the TSD propagation vectors by channel, showing wavefront
281 direction (vector angle) and propagation speed (vector magnitude). **(d)** Average speed of TSD
282 propagation by channel with standard error. Each TSD is depicted using a unique color matched
283 with panels e and g in this figure. **(e)** Absolute difference in direction between the XCaMP-Y and
284 RCatchER vectors during TSD. **(f)** Individual cell recruitment times by channel of the TSD
285 projected on to the propagation axis of XCaMP-Y. **(g)** Mean ER calcium change latency relative
286 to the cytosolic calcium change within cell during TSD across all recordings with pooled standard
287 error (left) and the distribution of these latencies for each recording (right). The effect of channel
288 on recruitment times used to compute these latencies are modeled using GLME (p=6.25×10^{-11},
289 N=4 recordings, 4 subjects with N=35-289 cell/recording). **(h)** Average individual cell changes in
290 calcium by compartment during TSD across recordings presented with pooled standard error. The
291 effect of event on calcium level are modeled using GLME (cytosol: p=0.234, ER: p=4.81×10^{-4},
292 N=3 recordings, 3 subjects with N=35-289 cells/recording). For all group level analysis (d, e, g,
293 h) N=7 recordings across 7 subjects with n=82-418 cells per recording. *p<0.05, **p<0.01,
294 **p<0.001.
295

296 **ER calcium depletion is a conserved feature across multiple types of CSD**
297 We next sought to determine if these calcium changes were specific to CSD in the context of
298 seizures or if they were a property of CSD itself. For this we used an electrical stimulation model
299 of CSD[39] where we stimulated through two epidural electrodes chronically implanted adjacent to
300 the recording field, while conducting the same imaging, EEG and DC recording paradigm we
301 employed earlier (Fig. 5a). By applying bipolar stimulation between the two electrodes (2 kHz,
302 100 µA, square wave, 10 s) we were able to reliably induce CSD (Supplementary Movie 2). The
303 DC shift during electrically evoked CSD was comparable to that during PTZ-induced CSD (Fig.
304 5b; -19.28±1.97 µV; mean ± SE; N=7 recordings, 7 subjects). Similarly, during the electrically
305 induced CSD we observed changes in calcium that paralleled PTZ-induced CSD, both in terms of
306 magnitude (Fig. 5C) and spatiotemporal pattern (Fig. 5d, e), albeit with the CSD propagating at a
307 faster speed, radially from the electrode pair. The cytosolic and ER calcium changes occurred with
308 the same velocities (Fig, 5f, g), with the ER depletion following the cytosolic increase (Fig 5h, i).
309 We observed a delay in the calcium changes relative to the DC shift consistent both with the
310 position of the imaging field relative to the simulating electrodes, and with the speed of
311 propagation (cytosol: 2.74±0.30 s; ER: 3.03±0.41 s). The durations of the calcium changes (Fig.
312 5j) were again consistent with the average duration of the DC shift (40.53±6.03 s, N=6 recordings,
313 6 subjects). In addition to the high frequency stimulation of long duration (2 kHz for 10 s), we
314 were able to induce CSD with short trains of stimulation of lower frequency, as typically used in
315 responsive neurostimulation (RNS) devices (Supplementary Fig. 4; N=3 subjects, 2 trials per
316 subject; 250-750uA [charge density within an order of magnitude of RNS range], 200 Hz, biphasic,
317 160 µs pulse width, five 100-ms trains with 5 s inter-train interval)[40, 41]. Thus, the intracellular
318 calcium dynamics observed during seizure associated CSD were also found with electrically
319 induced CSD, suggesting that the depletion of ER calcium is conserved across CSD.
320
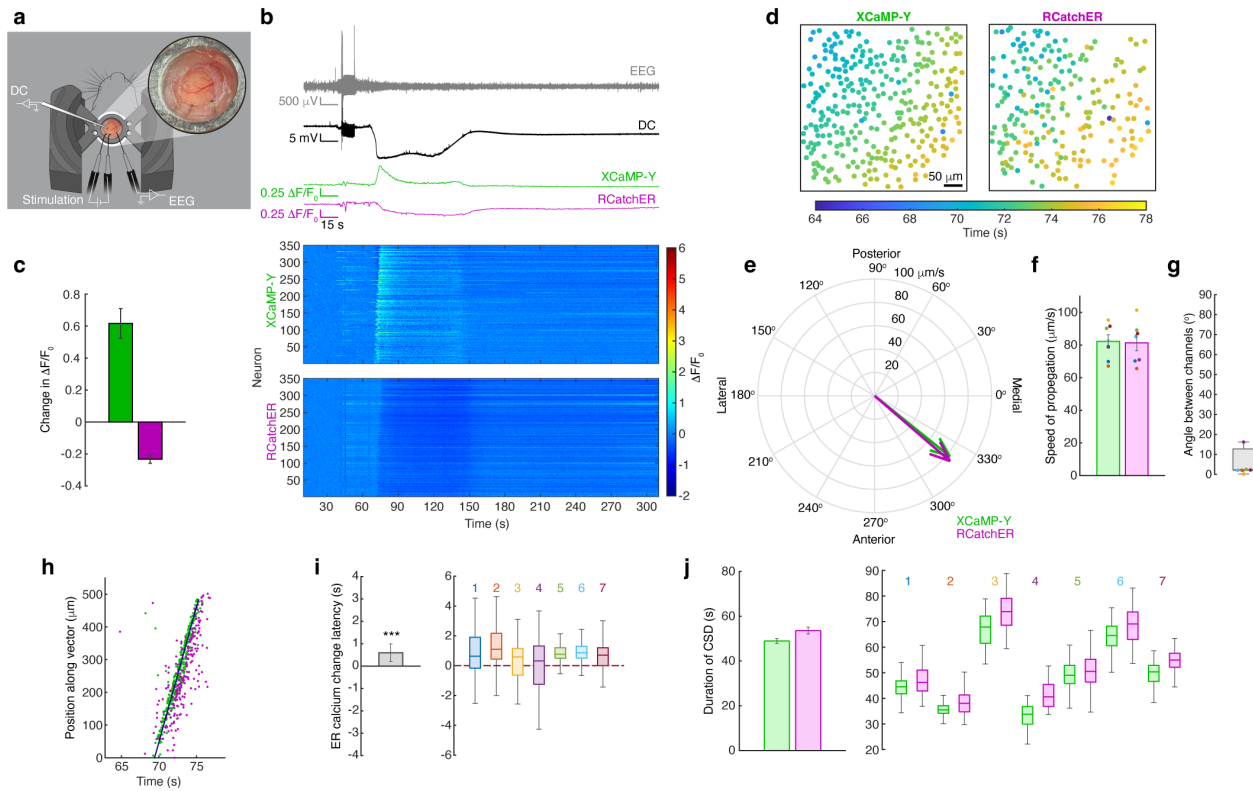
Figure 5. Spatiotemporal subcellular calcium dynamics during stimulation-induced CSD demonstrate ER depletion

(a) Illustration depicting the awake head fixed two-photon imaging along with simultaneous EEG and DC recording during stimulation-induced CSD. Expanded is an image of a cranial window with access port and electrodes for stimulation and EEG. **(b)** Mean population calcium fluorescence (XCaMP-Y: green, RCatchER: magenta) with synchronized EEG (grey) and DC (black) recordings during stimulation-induced (10 s) CSD from a representative subject. Note stimulation artifact at 30 s. Corresponding rasters of individual cell calcium transients (y-axis: neurons ordered from left to right across the field) are presented below. **(c)** Average individual cell changes in calcium by compartment during CSD across recordings presented with pooled standard error. **(d)** ROI colormap of determined recruitment times for identified cells during CSD, with color corresponding to recruitment time. **(e)** Polar plot of the CSD propagation vectors by channel, showing wavefront direction (vector angle) and propagation speed (vector magnitude). **(f)** Average speed of CSD propagation by channel with standard error. Each CSD is depicted using a unique color matched across all the panels in this figure. **(g)** Absolute difference in direction between the XCaMP-Y and RCatchER vectors during CSD. **(h)** Individual cell recruitment times by channel of the CSD projected on to the propagation axis of XCaMP-Y. **(i)** Mean ER calcium change latency relative to the cytosolic calcium change within cell during CSD across all recordings with pooled standard error (left) and the distribution of these latencies for each recording (right). The effect of channel on the recruitment times use to compute these latencies are modeled using GLME (p=4.63×10^{-8}). **(j)** Average duration of CSD within cell by channel across recordings with pooled standard error (left) and the distribution of the event lengths for each recording (right). For all group level analysis (c, f, g, i, j) N=7 recordings across 7 subjects with n=82-418 cells per recording. *p<0.05, **p<0.01, ***p<0.001.

11

347

Post-ictal activity decreases after CSD

CSD has been previously reported to arrest epileptiform activity in rodents[17]. We next sought to see if that observation held true for our generalized seizures. For this, we quantified spike wave discharges (SWDs) typically observed before and after seizures using our EEG recordings (Fig. 6a). We found that the SWD rate significantly decreased post-ictally when a seizure was followed by CSD, but not when a seizure occurred without a CSD (Fig. 6b; without CSD: p=0.383, N=8 seizures, 5 subjects; with CSD: *p=0.031, N=6 seizures, 5 subjects; Wilcoxon sign-rank test), suggesting a negative correlation between CSD and post-ictal epileptiform activity. To further test if CSD is sufficient to suppress epileptiform activity, we induced CSD using electrical stimulation 5 minutes into the post-ictal phase in a subset of seizures unaccompanied by a CSD (Fig. 6c). We found that, while the post-ictal SWD rate before electrical stimulation was not significantly different from the pre-ictal period (Fig. 6d; Friedman test post-hoc comparison; $p=0.7593$), following electrical stimulation evoked CSD, the SWD rate was significantly decreased (Friedman test with post-hoc comparison: *$p=0.0356$, $n=4$ seizures, 3 subjects). An innate gradual decline in post-ictal SWD rate could not account for this observed difference. We compared the recordings in the same time periods (5-10 minutes post seizure) without electrical stimulation and CSD and found there was no significant difference in SWD rate between the pre-ictal and the post-ictal period ($p=0.7422$; $n=8$ seizures, Wilcoxon sign-rank test). Taken together, CSD, whether it occurs naturally or evoked by electrical stimulation, has potential to diminish post-ictal epileptiform activity.

368
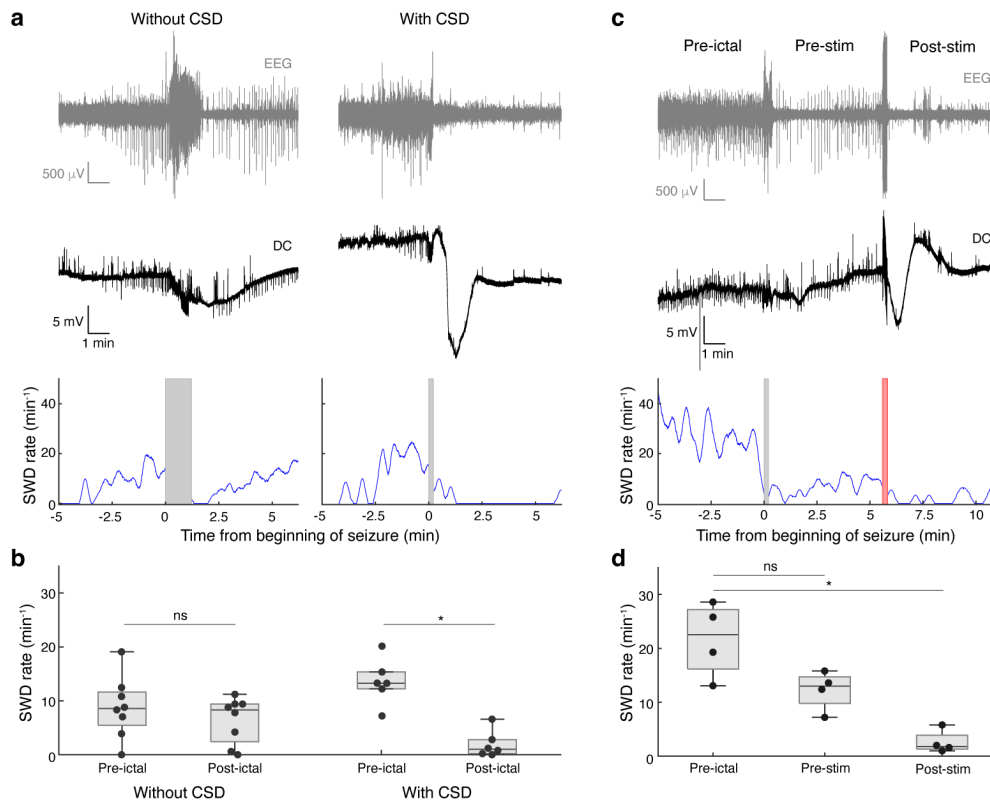
Figure 6. CSD is associated with suppression of epileptiform activity.

(a) Representative EEG (grey), DC (black) and SWD rates (blue) of the pre- and post-ictal periods for seizures occurring with and without CSD. SWD rate was not calculated during seizure (dark grey box). (b) Box plot comparing the SWD rate between the pre- and post-ictal periods with and without CSD. Wilcoxon sign-rank test was used. Without CSD: p=0.313, N=8 seizures, 5 subjects; With CSD: *p=0.031, N=6 seizures, 5 subjects. (c) Representative EEG (grey), DC (black) and SWD rate (blue) of the pre-ictal and post-ictal periods, during a seizure without naturally occurring CSD, where a CSD was electrically induced post-ictally. The post-ictal period is further delineated as before (pre-stim) and after stimulation (post-stim). SWD rate was not calculated during seizure (dark grey box) or stimulation (light red box). (d) Box plot comparing the SWD rate between the pre- and post-ictal periods (both pre-stim and post-stim) during seizures without naturally occurring CSD, where a CSD was electrically induced. Friedman test with post-hoc comparison was used. *p=0.0356, N=4 seizures, 3 subjects.

DISCUSSION

In this study we introduce our XCaMP-Y-P2A-RCatchER imaging construct, for simultaneous *in vivo* two-photon calcium imaging in the cytosol and ER (Fig. 1). RCatchER has previously only been used *in vitro*[34]. Here we expanded the utility of RCatchER by incorporating it into this multi-compartment *in vivo* imaging approach, a novel vertebrate intravital application of calcium imaging to the ER. The ability to capture rapid ER dynamics in awake animals opens vast possibilities for investigators, made all the more accessible through our single AAV design for multicompartment two-color imaging. We envision the usefulness of our construct extending across the biological sciences, from immunology for the study of lymphocyte activation[42], to cardiology for examining cardiomyocyte contraction[43].

To demonstrate the utility of *in vivo* RCatchER, we apply this paradigm to a rodent seizure model, which enabled us to uncover ER calcium dynamics unique to CSD. Principally, we observe a depletion of ER calcium occurring during post-ictal CSD (Fig. 2) and electrically induced CSD (Fig. 5) that does not occur during seizures themselves. Depletion of ER calcium was delayed by a few seconds relative to a cytosolic calcium increase, suggestive of CICR (Fig. 3). We observed comparative delays in depletion of ER calcium in TSD (Fig. 4) as well as in electrically evoked CSD (Fig. 5). We also present further evidence of the influence of CSD on seizures, with a focus on the post-ictal suppression of epileptiform activity that correlates with CSD occurrence, which was also recapitulated through electrically evoked CSD (Fig. 6). This suggests post-ictal suppression through CSD may serve as an innate therapeutic mechanism[17] and also raises the possibility of CSD as a therapeutic electrical stimulation etiology.

Given the potentially fast intracellular dynamics at play during CSD, we selected RCatchER for our paradigm to maximize our temporal resolution, while also permitting simultaneous cytosolic imaging. The vast majority of calcium indicator proteins, including XCaMP-Y, are based on EF-hand motif calcium binding domains, as is the case with the calmodulin of GCaMP[44], which require cooperative binding and consequently exhibit non-linear fluorescence dynamics[33, 45]. However, RCatchER has a unique calcium sensing mechanism, where a single calcium binding site was engineered on the surface of the scaffold of a red fluorescent protein, mApple[34]. This enables calcium ion binding with 1:1 stoichiometry without cooperativity, whereby its change in fluorescence is not limited by a slow conformational change. Consequently, RCatchER is an exceptionally fast acting calcium sensor, whose dissociation kinetics exceed the

13

temporal resolution of stopped-flow fluorescence measurements, while maintaining fluorescence outputs linear to the calcium levels. This ideally positions RCatchER to capture ER dynamics.

Combining our dual-color imaging approach with simultaneous EEG and DC recording we were able to capture single-cell neural activity and calcium homeostasis dynamics across hundreds of neurons in awake mice during PTZ-induced seizures and subsequent slow propagating calcium waves. It is known that CSD can follow or interrupt seizures[17, 21]. Large calcium increases propagating as traveling waves have also been observed during CSD[31, 46]. Similar calcium increases[47], and traveling waves[48-50] have been observed following seizures. While some have inferred that these calcium waves are therefore indicative of CSD, here we offer definitive proof of this association by corroborating these calcium waves with DC recordings.

An association between seizure and CSD occurrence has been demonstrated since early investigations into CSD. Studies from the 1950s in anesthetized rabbit cortex showed that electrically induced after-discharges, as well as PTZ-induced epileptiform activity could be followed by slow potential changes and CSD[51, 52]. The authors hypothesized that the SD was serving to arrest the seizures. They also noticed that the intensity of the epileptiform activity was typically less in tissue that had experienced a prior CSD, indicative of a potential protective consequence of CSD. These ideas are furthered by a PTZ kindling study in rats, where the investigators found that with kindling the occurrence of CSD decreased while the occurrence of epileptiform activity increased[20]. They, too, postulated that the CSD was arresting the seizure, but added that as kindling progressed, between the evolution to a more gradual seizure onset and upregulation of potassium reuptake mechanisms, the increase in extracellular potassium became less abrupt and thus the probability of CSD occurrence decreased, in turn arresting fewer seizures. They also noted a decrease in interictal spiking following CSD, a finding consistent with our results here. Induction of CSD has also been demonstrated to suppress spike wave discharges[53, 54] and seizures[17] in animal models, findings concordant with our demonstration of electrically induced CSD decreasing post-ictal spiking (Fig. 6).

The large rise in intracellular calcium we observed during seizures and CSD could itself have implications for seizure termination. During seizures, membrane depolarization opens voltage gated calcium channels and releases magnesium block of calcium-permeable NMDA glutamate receptors (NMDARs), which - coupled with excessive extracellular accumulation of glutamate - causes a large and rapid influx of calcium. This results in acidification of the intracellular compartment through the exchange of calcium and protons across the Ca^{2+}/H^+ ATPase. This acidification, in turn, can lead to decreased conductance of voltage and ligand gated channels[23]. As such, the acidification during a seizure has been hypothesized to promote seizure termination. Additionally, excessive activation of ATPase would contribute to the depletion of ATP, another potential component of seizure termination. Furthermore, the increase in intracellular calcium will lead to excessive neurotransmitter release and eventual depletion of synaptic vesicles, another potential factor in seizure termination[32]. The same processes occur during CSD[55, 56], although to a much greater extent. The intracellular calcium concentration is estimated to rise to 6-25 μM during CSD[7, 57], an order of magnitude greater than the rise of calcium during seizures (700 nM)[23, 58]. In this study, we observed a significant release of ER calcium during CSD, but not during seizures (Fig. 2). It is possible that this large ER calcium release specific to CSD is contributing to the higher cytosolic calcium concentration compared to that during a seizure, which could be a factor in the anti-seizure effect of CSD[17].

Our finding that the depletion of ER stores follows the increase in cytosolic calcium, presumably through voltage gated calcium channels and NMDARs, is suggestive of a CICR

14

occurring within neurons. While RCatchER and XCaMP-Y differ vastly in their kinetics, such a difference in the sensors in and of themselves cannot explain the delay, with the kinetics of RCatchER far exceeding those of XCaMP-Y. Calcium release from ER stores is mediated through two receptor families, ryanodine receptors (RyR) and inositol (1,4,5)-triphosphate (IP3) receptors. While IP3 is implicated in a variety of cell signaling cascades, RyR activation is more specific[3]. The RyR1 isoform, which has minimal expression in nervous tissue, demonstrates voltage dependence, mediated by a mechanical interaction with voltage dependent calcium channels. RyR2, which is the isoform predominantly expressed in the cortex, is activated through calcium influx and is voltage independent[59, 60]. The RyR response to calcium is biphasic, where they are activated at around ~1 μM of calcium and are subsequently inactivated when calcium exceeds ~1 mM[61-63]. The calcium dependence of RyR activation may explain our finding that depletion of ER calcium was small and insignificant during seizures, perhaps because intracellular calcium does not reach RyR activation levels, whereas in CSD, it exceeds this threshold. Furthermore, voltage dependent activation occurs faster (~2 ms) than the CICR, and while the activation of the RyR channel is relatively fast (<10 ms) in the immediate presence of sufficiently high calcium, the widespread induction of CICR is slower, being dependent on the rate of calcium influx and diffusion through the cytosol[2, 63]. IP3 mediated calcium release can also occur over a similar timeframe. As calcium is a co-agonist for the IP3 receptor and considered the driving force behind larger concerted calcium releases, such as the one we observe here, this would also support the CICR hypothesis, albeit by an alternate pathway[64]. Thus, the relative recruitment dynamics we observe during CSD are temporally corroborative with a CICR, although further investigations are needed to identify the precise receptors at play.

Following ER depletion, store operated calcium entry (SOCE) can occur through calcium release activated channels (CRACs) at the cell plasma membrane, including the ORAI1/STIM1 complex, further increasing cytosolic calcium[65-67]. While NMDARs have been considered the primary route of entry contributing to the large increase in cytosolic calcium during CSD[68], SOCE could be contributing to the sustained increase in cytosolic calcium observed in CSD.

Gain of function mutations causing 'leaky' RyR2 have been linked to SUDEP, with knock-in studies of the same mutated receptors in rodents demonstrating decreased threshold for seizures and CSD[69]. While the effects of this mutation could be upstream of CSD by promoting cortical excitability, it could also be directly impacting the generation of CSD, particularly if CICR or SOCE are central to the CSD mechanism rather than only downstream consequences.

While we were able to make a comparison of the timing of cytosolic increase to ER calcium depletion at the start of CSD, it was more difficult to make such a comparison for the offset of the CSD. This is primarily due to the gradual and often smaller calcium changes occurring at the end of the CSD, leading to less precision in the selection of an offset time. However, this variability is small when compared with the length of CSD and with the offset event duration across the population and thus does not dramatically impact the spatial regression for these slow traveling waves. Mechanistically, irrespective of the imprecision in measurement, the timing of these two events are within an acceptable range for the expected timing of cytosolic calcium return to the ER through the sarco(endo)plasmic reticulum ATPase (SERCA) pump[70].

It is important to note that other ER dynamics are occurring during CSD aside from the observed calcium depletion that could have implications for our findings. ER is known to undergo morphological change during CSD: fission and fragmentation of ER occurs in a calcium calmodulin-dependent kinase II (CaMKII)-dependent manner[46], which can potentially contribute to the RCatchER signal we measured in this study. However, we deduce that the ER calcium signal

15

509 we measured in this study was not significantly affected by the morphological change of ER due
510 to the slow nature of ER fission and fusion. The RCatchER signal decreased within a second of
511 the increase in cytosolic calcium (Fig. 3), whereas the ultrastructural changes in the ER were found
512 to occur several seconds after the calcium influx, indicating that the ER calcium release precedes
513 the fission. Additionally, the RCatchER signal recovered within a minute following the depletion
514 of ER calcium (Fig. 3), while the ER fusion should take several minutes to restore continuity of
515 ER. Even if ER is fragmented into beaded structures, that by itself should not hinder the calcium
516 dependence of RCatchER fluorescence. Furthermore, the ER beading occurs predominantly in the
517 neuropil, while our imaging analysis primarily focused on somata. Given the calcium dependence
518 of CaMKII, perhaps the release of ER calcium stores we describe here facilitates the fission event.

519 Another consideration for our finding is the potential impact of intracellular pH on
520 RCatchER's excitability. While intracellular acidification does occur during seizures, the time
521 course is a gradual change throughout the seizure and continuing during the post-ictal phase[71],
522 rather than an abrupt drop post-ictally. During CSD acidification also occurs although there is a
523 delay in the drop in pH relative to the DC shift and the pH decrease is sustained for longer than
524 the DC shift[72-74]. Therefore, the dynamics we observe here are not temporally concordant with the
525 pH changes observed. Furthermore, the ER is well buffered, having little change in pH during
526 calcium release and experiences much smaller magnitude pH changes than the cytosol during
527 intracellular acidification[75].

528 TSD is an anoxic variant of CSD occurring during death[76, 77], known to have slightly
529 different mechanisms underlying its calcium dynamics. However, we still observed a depletion of
530 ER calcium stores following a large cytosolic increase, albeit more delayed. Under severe hypoxia,
531 hyperpolarization as a nonspreading depression occurs in the brain, observed as an isoelectric
532 EEG, preserving the ATP stores necessary for recovery. If, however, the hypoxic conditions last
533 more than a few minutes, the ATP stores become depleted, the ion gradients across the membranes
534 break down, and a TSD is, in turn, initiated[7, 55]. While calcium and NMDAR have been found to
535 be necessary for CSD occurrence in normoxic conditions, in the context of hypoxia, CSD can
536 occur in the absence of extracellular calcium and NMDAR function[57, 78, 79]. We observed such
537 TSD calcium waves after about a minute of isoelectric EEG during fatal seizure recordings (Fig.
538 4). While the propagation patterns were similar to CSDs in surviving animals with respect to
539 overlapping direction and speed, the delay in the ER depletion following the increase in cytosolic
540 calcium was slightly longer during TSD. The increase in cytosolic calcium fluorescence was
541 smaller during TSD than other CSD, perhaps contributing to this longer delay in a CICR.
542 Consistent with cell death and ATP depletion, the cytosolic calcium increase was sustained, and
543 ER calcium was not restored. While cells can typically tolerate the length of depolarization and
544 elevated calcium during a seizure or normoxic CSD[55], with some neuroprotective effect even
545 having been demonstrated for the intracellular calcium concentrations reached during seizures[80,
546 81], the levels experienced during CSD when sustained, as is the case in anoxia and TSD, are
547 generally regarded to be toxic[3, 68].

548 Our findings support the plausibility of calcium homeostasis dysregulation during CSD.
549 However, further investigation is needed to determine the necessity of CICR in CSD and its seizure
550 suppressive effect. If CICR proves to be mechanistically involved, evidence of its exact mediators,
551 be it RyR or IP3 dependent, could provide us with new targets for modulation, informing our anti-
552 epileptic arsenal. While CSD may be beneficial in the context of widespread aberrant brain activity
553 during a seizure, it can most certainly have pathologic consequences. Being able to mimic the anti-
554 seizure effect of CSD while avoiding its toxic side effects could offer great therapeutic potential.

16

555 Alternatively, if CICR rather contributes to the prolonged depolarization and toxic consequences
556 of CSD, prevention of this calcium store depletion during CSD could also be of benefit.
557   The clinical implications of our investigation afford insight not only to potential
558 neuromodulatory targets, but also to hypothetical mechanisms underlying established therapeutics,
559 namely electrical stimulation used for seizure control. Notably, we were able to induce CSD using
560 different stimulation parameters, including ones paralleling typical RNS settings. Indeed, repeated
561 cortical stimulation has been shown to cause increases in extracellular potassium, likely
562 contributing to CSD induction[82]. The clinical benefits of RNS are likely multifaceted. In large part
563 the decreased seizure incidence is hypothesized to be mediated by neuroplasticity[83], rather than
564 direct arrest of seizures, as seizures in most patients are not terminated by RNS, and the majority
565 of stimulation occurs interictally. However, in those patients for whom seizures are arrested, these
566 results raise the possibility that CSD could be occurring and contributing to the suppressive effect.
567
568 **MATERIALS AND METHODS**
569
570 **Molecular Biology**
571 An AAV2 transfer plasmid containing the XCaMP-Y-P2A-RCatchER cassette was generated
572 through standard molecular biology (restriction enzyme [RE] digestion, ligation, transformation,
573 and plasmid purification). The RCatchER cassette in the pcDNA3.1 vector[34] was cut with NheI
574 and EcoRV and ligated into the NheI and blunted HindIII RE sites in an AAV2 transfer vector
575 with the human synapsin I (hSynI) promoter (Addgene plasmid number: 100843), resulting in
576 pAAV2/hSynI-RCatchER. The coding sequence of XCaMP-Y[33] (GenBank accession number:
577 MK770163.1) was fully synthesized through a commercial service with an NheI RE recognition
578 site added at the 5' end (gBlocks gene fragments, Integrated DNA Technologies). The NheI and
579 ClaI fragment of XCaMP-Y was ligated together with the ClaI and BamHI fragment of separately
580 synthetized P2A sequence into the respective RE sites upstream of RCatchER, resulting in
581 pAAV2/hSynI-XCaMP-Y-P2A-RCatchER. The correct sequence was confirmed through RE
582 analysis, as well as Sanger and next-generation sequencing (Eton Biosciences and Plasmidsaurus,
583 respectively). Endotoxin-free DNA was obtained through a commercial midiprep plasmid
584 purification kit (NucleoBond Xtra Midi EF, Takara Bio USA).
585
586 **Viral Vector Production**
587 We produced a recombinant adeno-associated viral (rAAV) vector pseudotyped with AAV9 capsid
588 protein in-house following a modified standard procedure[84]. In brief, we transfected human
589 embryonic kidney 293FT cells (Invitrogen) with three plasmids (helper [Addgene plasmid number:
590 112867], AAV2/9 rep/cap [Addgene plasmid number: 112865], and pAAV2/hSynI-XCaMP-Y-
591 P2A-RCatchER) at 1:1:1 molar ratio using the calcium-phosphate method. We then harvested the
592 rAAV, purified through iodixanol gradient ultracentrifugation, and concentrated in Dulbecco's
593 phosphate-buffered saline (D8537, Millipore-Sigma) supplemented with 0.001% (v/v) Pluronic F-
594 68 (Millipore-Sigma). We aliquoted and stored it at -80°C until surgery. Using quantitative PCR,
595 we determined the titer to be 4×10^{14} viral genomes/mL.
596
597 **Cranial Window Fabrication**
598 To generate windows for chronic imaging with the capability for repeated access via a pulled glass
599 micropipette electrode for DC recording, we adapted protocols for concentric window design[85]
600 with single plane windows along with silicone access ports[86, 87]. We used two smaller inner layer

17

601 coverslips and one larger outer layer coverslip (3 mm and 5 mm diameter, respectively, #1
602 thickness, Warner Instruments), and generated a 0.7 mm diameter access port placed 0.75 mm
603 from the center (Supplementary Fig. 1a). When deciding on diameter of the window it is important
604 to consider the planned angle of penetration for the recording electrode, along with the thickness
605 of the electrode and depth of the access port so as to ensure the window has a large enough diameter
606 to accommodate these constraints (Supplementary Fig. 1b). We began by first etching the holes in
607 each glass layer at the correct coordinates to ensure the holes alignment (0.75 mm from the side of
608 the 3mm glass and 1.75 mm from the edge of the 5mm glass) when the glass layers are stacked
609 concentrically. For etching we suspended the glass using a spring hinged clip to apply light, but
610 sufficient pressure to the edges of the cover glass. To protect the glass from damage, we covered
611 the clip with heat shrink wrap. Using a conical sharp tip fine grit stone grinding burr (CA1063,
612 Minimo Precision Instruments and Tools) with a dental handpiece at a medium speed (~6000-7000
613 rpm), we slowly hand dry etched each cover glass at a 45° angle, moving halfway through each
614 piece of glass from each side to meet in the center, with applying dust free air routinely to clear
615 away the silicone dust during etching. Upon meeting in the center, we moved the burr into a
616 vertical position (perpendicular to the cover glass) to round out and straighten the beveled edges
617 from both sides of the glass as needed to minimize imaging artifacts. We then cleaned each cover
618 glass with lens paper and compressed air.
619   We next assembled the cover glass using optical adhesive (Optical Adhesive 71, Norland),
620 on a Styrofoam platform with vertical pins (000 insect pins; 0.5 mm shaft diameter) to thread the
621 holes for cover glass alignment. We adhered the layers serially using a small amount of adhesive
622 (just enough to spread to the edge of the 3mm glass), first the 5mm to a 3mm and then the second
623 3mm to the first, with interleaved UV curing (365 nm; wavelength of peak absorbance) for 30 min.
624 We then cured overnight (>12 h) at 50°C. The optical adhesive must be uniformly distributed
625 between articulating surfaces to prevent thin film interference.
626   The final step is to prepare the silicone membrane by filling the access port with optically
627 transparent silicone (Sylgard 184, Dow Corning), selected because it can be cured at room
628 temperature given the initial limited temperature range tolerance of the optical adhesive (-15-
629 60°C). We prepared the silicone at a 10:1 mixture by weight of base to catalyst. Next, we increased
630 the viscosity of the silicone through heating to facilitate easier application to the port using heat
631 gun at 150-200°C for about a minute. Then using a 30-gauge insulin needle we applied a tiny drop
632 of the prepared silicone to fill the access port of the windows while suspending them in mid-air by
633 their edges with light tension to prevent wicking. We then transferred the suspended windows to
634 a vacuum chamber and cured at room temperature for two days to prevent bubble formation in the
635 silicone. We then followed this with a one-day cure at 50°C. Curing at a higher temperature
636 increases the silicone's strength (higher shear modulus), while curing at a lower temperature
637 increases its elasticity (lower strain at break)[88]. We designed this approach to ensure a balance of
638 strength and elasticity such that the membrane will not deform under increased intracranial
639 pressure (strength), while at the same time will properly re-seal upon needle withdrawal
640 (elasticity). We stored these windows at room temperature. For a full cure we waited an additional
641 four days and implanted them within a few months, before the silicone dried out, becoming more
642 brittle and losing its elasticity.
643
644 **Stereotaxic Surgery**
645 All procedures involving live animals were conducted with approval from and in accordance with
646 Emory University's Institutional Animal Care and Use Committee. Adapting standard protocols

18

647 for concentric cranial window implantation[85, 89], we performed stereotaxic cranial window surgery
648 on adult (≥ 90 day-old) albino C57BL6/N male mice (B6N-*Tyr^c-Brd*/BrdCrCrl, Charles River,
649 Strain Code 493) concurrently with intracortical delivery of rAAV, electrode placement for
650 recording and stimulation, and headplates affixation. In brief, we secured the mice in a stereotaxic
651 frame and maintained them under anesthesia (1.5% isoflurane balanced in oxygen (1 L/min)). We
652 then performed a 3 mm craniotomy over the primary motor cortex. Two injections of rAAV (500
653 nL each; 2 nL/s) were performed through a pulled glass capillary tube (Nanoject 3.0, Drummond)
654 at 300 μm and 600 μm deep to the pial surface (0.30 mm anterior and 1.75 mm lateral to Bregma)[90,
655 91]. We then epidurally placed a thin polyamide insulated tungsten wire electrode with exposed tip
656 (125 μm; P1Technologies) at the posteromedial edge of the craniotomy, along with ipsilateral
657 reference and contralateral ground stainless steel screw electrodes (E363/96/1.6/SPC,
658 P1Technologies) in the skull over the cerebellum (0.7 mm burr holes). If the mouse was to be used
659 for stimulation as well, we also placed two additional wire electrodes (same material and size)
660 epidurally about half a millimeter apart along the posterolateral edge of the craniotomy. We
661 prefabricated all electrodes with gold pins to facilitate easy attachment to a recording preamplifier
662 or stimulus isolator. We next placed a cranial window to plug the craniotomy and affixed the
663 window and electrodes to the skull using dental acrylic (C&B Metabond, Parkell) along with a
664 stainless steel headplate (Models 3 and 4; Neurotar). We closed the skin to headplate using tissue
665 adhesive (Vetbond, 3M).
666
667 **Two-Photon Imaging and Electrophysiology**
668 We performed resonant scanning (30 Hz, 512x512 pixels) two-photon imaging on mice during
669 acute induced seizures. We used a two-photon microscope (HyperScope, Scientifica) equipped
670 with a pulsed tunable infrared laser system (InSight X3, Spectra-Physics) and controller software
671 (ScanImage, Vidrio Technologies). We selected 1000-1010 nm wavelengths for excitation (Fig.
672 1C) and separated the emissions by a dichroic mirror (565LP, Chroma) with band pass filters
673 (ET525/50m-2p and ET620/60m-2p, Chroma), collecting the light using GaAsP and multi-alkali
674 red-shifted photomultiplier tube, respectively. Beginning one month following surgery to allow
675 for adequate GECI expression, we head-fixed the mice in a carbon fiber airlifted chamber (Mobile
676 HomeCage, Neurotar), positioned under a long working distance 16x objective (water-immersion,
677 N.A. 0.80, Nikon). We connected the EEG electrodes to an AC preamplifier and a data acquisition
678 system (Sirenia, Pinnacle Technologies). For DC recording, on the day of a recording session, a
679 reference electrode (1-mm diameter Ag/AgCl pellet, Model E205, Harvard Apparatus) was placed
680 in the nuchal muscle of the mouse under isoflurane anesthesia. A micromanipulator (Kopf
681 Instruments) was affixed to the crossbar of the headplate holder. We stereotaxically inserted a
682 long-shank pulled glass electrode (1 mm diameter with ~70 μm at the tip, $1 - 3$ MΩ when filled
683 with the following solution: 125 mM NaCl, 2.5 mM KCl, 1.25 mM NaH_2PO_4, 26 mM $NaHCO_3$,
684 20 mM d(+)-glucose, 2 mM $CaCl_2$, and 1.3 mM $MgCl_2$) through the access port at a 45° angle into
685 the cortex to a depth of 100-300 μm below the pial surface. DC signals were recorded through a
686 patch clamp amplifier, a digital data acquisition system, and software (MultiClamp 700B, Digidata
687 1550B, and pClamp, respectively, Molecular Devices). Both EEG and DC signals were recorded
688 at 2 kHz, with a 0.5-300 Hz bandpass filter for the EEG and with a 500 Hz low-pass filter for the
689 DC recordings. EEG was continuously recorded while DC recording and two-photon imaging were
690 triggered by a TTL pulse generated in the EEG recording system immediately before either PTZ
691 injection or electrical stimulation.
692

19

Acute Seizure Model

We subcutaneously injected PTZ (40-50 mg/kg; P6500, Millipore-Sigma; sterile saline diluent) and recorded for 20-45 min depending on the course of the seizure. All but one PTZ injection resulted in at most one generalized seizure per recording session. We performed multiple seizure experiments within the same subject provided the seizures were not fatal, with sessions separated by at least a week to circumvent the effects of kindling[92].

Electrical Stimulation

We performed electrical stimulation using a waveform and function generator (EDU33210A Keysight, USA) to drive a stimulus isolator (DS4 or DS5, Digitimer, UK) attached to the chronically implanted electrodes. Typical stimulation parameters were 50% duty cycle bipolar pulses with amplitudes of ±200 µA at 2 kHz for 10 s. We stimulated the mice 30-40 s following the start of image acquisition and would acquire 10-15 min of data depending on the course of the CSD. To evaluate the threshold for inducing CSD with RNS style parameters we created waveforms in MATLAB and then used the generator to drive them. We began stimulation at the lowest setting and proceeded to increase current with each subsequent stimulation periods (25, 50, 100, 250, 500 and 750 µA) until CSD was induced, interwoven by 2-minute washout periods. Following CSD we had a 20 min washout before the trial was repeated within the same subject.

For post-ictal simulation-induced CSD experiments we performed electrical stimulation using the same approach as above in a subset of animals during seizures occurring without CSD. In these recordings we waited 5 min following the end of the seizure to ensure a CSD did not occur naturally and to acquire a baseline post-ictal spiking. We then stimulated to induced CSD and recorded for at least an additional 5 min.

Histology

Following experiments, all subjects underwent transcardial perfusion (4% paraformaldehyde (PFA) in phosphate buffered saline (PBS), 4°C; 32% PFA stock solution, Electron Microscopy Solutions, cat no. 15714) and their brain tissue was extracted. The brains were further fixed overnight in 4% PFA (4°C) and then cryoprotected for 36 hours in 30% sucrose (in PBS, 4°C). The tissue was serially sectioned using a freezing microtome (Spencer Lens Co. equipped with a Physitemp BFS-40MPA Controller and platform) at 40 µm thickness (coronal) and stored in PBS at 4°C.

For triple immunofluorescence, free-floating sections were rinsed in PBS, blocked in PBS solution containing 4% normal donkey serum (NDS), 4% normal goat serum (NGS) and 0.1% Triton-X for 30 minutes at room temperature. After rinses in PBS, sections were then incubated overnight at 4°C with a combination of chicken anti-GFP (1:100, GFP-1020, Aves Labs, Davis, CA, USA), mouse-anti-mCherry (1:200, AE002, Abclonal, Woburn, MA, USA), and rabbit anti-SERCA2 (1:50, A1097, Abclonal, Woburn, MA, USA) in PBS containing 2% NDS and 2% NGS. Sections were rinsed in PBS and incubated in a PBS solution containing Alexa Fluor 488-conjugated goat anti-Chicken IgG (1:1000, Invitrogen A-11039, ThermoFisher Scientific, Waltham, MA, USA), Alexa Fluor 594-conjugated donkey anti-mouse IgG (1:1000, 715-585-150, Jackson Immunoresearch Laboratories, West grove, PA, USA) and Alexa Fluor 647-conjugated goat anti-rabbit IgG (1:500, 111-607-008, Jackson Immunoresearch Laboratories, West grove, PA, USA) secondary antibodies and 2% NDS/2% NGS for 1 hour at room temperature. Sections were rinsed with PBS, then mounted on glass slides, dried and cover slipped with hard set mounting medium containing the nuclear marker, DAPI (Vectashield, H-1500, Vector Laboratories,

739 Burlingame, CA, USA). Images were captured using a Leica SP8 upright confocal microscope
740 and LASX software. Immunofluorescence image processing, including projections and orthogonal
741 view generation, was performed using FIJI[93].

742

Image Processing

744 We performed imaging pre-processing using the Suite2P software package[94] with integrated
745 Cellpose[95], performing motion registration, region of interest (ROI) detection and calcium
746 transient extraction of soma and surrounding neuropil. We additionally manually curated the
747 candidate ROIs to ensure they were from cell bodies and not overlapping with any major blood
748 vessels. We background subtracted the raw fluorescence traces taking the global minima of the
749 neuropil transients for each recording as a proxy for the background signal. We also generated
750 clean somatic signal by subtracting 70% of the surrounding neuropil signal from the somatic ROI
751 signal to remove out-of-plane contamination[94] and adjust for photobleaching. We normalized the
752 traces as $\Delta F/F_0$, using the mean of the first 30 s of recording as baseline fluorescence (F_0). Finally,
753 we double-reverse filtered the traces using an adaptive filtering routine (1 Hz, Butterworth lowpass
754 filter, order 3 to 5) that preserves the phase of the signal prior to processing.

755

Data Analysis

757 For baseline recording spike detection we employed a peak detection heuristic to select all
758 transients at least four standard deviations above baseline. We computed the average spike trace
759 with pooled standard deviation, aligning all the detected transients by their point of maximum
760 slope. The change in calcium level during each spike was taken as the difference between the
761 average signal during half-second windows before and after the recruitment time.
762   For recruitment time detection during seizures, we used our previously reported automated
763 approach[28]. In brief, the approach uses the mean population calcium trace along with EEG (in this
764 study we also used DC) to find PIS, seizure and CSD onsets in the recordings and defines detection
765 windows around these events. It then searches the individual traces within these windows for local
766 maxima in the integral of their slope, indicative of rapid and sustained increases in cytosolic
767 calcium that occur during recruitment to these seizure related events. These increases must exceed
768 an event and channel specific threshold above baseline for the cell to be considered recruited to
769 the event. All individual cell recruitments are then indexed by the point of steepest slope, being
770 generally accepted as a recruitment time for seizures[96, 97], and the point least likely to be perturbed
771 by filtering. For processing the RCatchER signal, we inverted the transients, enabling our
772 algorithm, originally designed to find increases in cytosolic calcium, to find the decreases in signal.
773 With the majority of recordings and events we used the clean somatic traces for detection. We also
774 adapted this method to determine recruitment times of CSD offset. However, due to lower signal-
775 to-noise ratio during the offset of CSD and during TSD, we needed to use the somatic traces before
776 neuropil subtraction for event detection. Additionally, for determining the offset of CSD a few
777 modifications to the approach were implemented given the gradual rather than rapid nature of the
778 change being measured. Namely we filtered the traces to 0.05-0.1 Hz and searched for the local
779 minima/maxima of concavity to estimate the beginning of the offset calcium change.
780   To determine the magnitude of calcium changes in individual cells during seizures and
781 CSD (including TSD), we computed the difference between the average signal during ten and five
782 second windows, respectively, before and after the recruitment times. For the calcium change
783 during the recruitment to PIS, we also computed the difference in calcium levels before and during
784 the spike. However, we found that using the average signal diminished the amplitude of change

21

785 too much and using only the maxima left the values too subject to shot noise. Therefore, we opted
786 to further filter the traces to 0.5 Hz before taking the maxima during a one second window before
787 the spike to compare with a two second window encompassing the full spike. To determine the
788 impact of event (PIS, seizure or CSD) on calcium change we model the calcium changes using a
789 GLME with effects coding and with each recording session modeled as a random effect. Then to
790 evaluate the if there was a sustained post-ictal calcium change in an unbiased way, we determined
791 the average post ictal calcium signal in each cell over a sliding 15 s window for each seizure
792 recording. Then using the same GLME approach we modeled the impact of CSD on the post-ictal
793 calcium.
794   For determining vectors of propagation, as we previously demonstrated[28] we applied a
795 spatial linear regression algorithm, with L1 regularization (originally developed to model interictal
796 events in human intracranial data)[37, 38], to our data, using the positions of the cells withing the field
797 and the determined event recruitment times. We only considered statistically significant vectors
798 (p<0.05; although for nearly all of the vectors p<0.001) in our analysis, where p-values were
799 computed by comparing model residuals to spatially shuffled data sets, as in prior work [37]. Speed
800 and direction of propagation were taken from these vectors for comparisons within and across
801 channels. The same recruitment times used to determine these vectors were also used to compare
802 the relative timings of recruitment to these events across channels, modeling the effect of channel
803 on recruitment time using a GLME with effects coding and with each recording session modeled
804 as a random effect.
805   For computing the DC shift onset and offset we first smoothed the DC trace using a rolling
806 average, downsampling and interpolation. We took the local minima near the DC fall and local
807 maxima near the DC rise of the second derivative of the trace as the onset and offset times,
808 respectively. We used these times to compute the DC shift period lengths and latencies with respect
809 to the calcium changes.
810   We produced all movies and time-lapse representative frames from the motion registered
811 image stacks output of Suite2P processed using FIJI[93]. We filtered the stacks using a 3D gaussian
812 filter (X-Y: 0.5 standard deviation (SD); time: 1 SD) and down sampled to 6 Hz (movie) or 1 Hz
813 (representative frames) using bilinear interpolation.
814   To examine the SWD rates in EEG, we used a bandpower-based threshold detection
815 method[28, 98] to find all EEG spikes in a recording. We then divided the recordings into the specific
816 periods we wished to compare. We used the same pre-ictal period as in the calcium data. We then
817 used Welch's power spectral density to compute a spectrogram and used specific frequency
818 features to define the boundaries of the post ictal time periods being compared. The post-ictal
819 period began at the end of the seizure, defined as the point when the total power (<100 Hz) fell
820 below 5% of the maximum power achieved during the seizure. For recordings without post-ictal
821 stimulation, we ended the period 5 min later, being equivalent to when we would induce CSD in
822 the post ictal stimulation recordings. For recordings with post-ictal stimulation, we defined the end
823 of the post-ictal/pre-stimulation period as the point where a stimulation artifact EEG power (50-
824 70 Hz & 170-190 Hz) crossed 50% of its maximum power. The post-ictal/post-stimulation period
825 began when the stimulation artifact power fell below 50% of its maximum and ended 5 min later.
826 We computed SWD rates by dividing the totals spike counts during each of these periods by their
827 length of time. We then computed moving-average SWD rate curves (Fig. 6 a-b) by convolving a
828 30 s-wide Gaussian window with a binarized array of detected spike times at the original signal
829 sampling rate. Statistics were performed using non-parametric pairwise tests, namely the Wilcoxon

22

830 sign-rank test for comparisons of two groups and the Friedman test for comparisons of more than
831 two groups.
832
833 **Two-photon Excitation Spectra**
834 For determining the excitation spectra of the two indicators, we imaged a mouse prepared for *in*
835 *vivo* imaging, expressing both XCaMP-Y and RCatchER, using the same approach as above,
836 except with galvo scanning (1.07 Hz, 512x512 pixels). We collected images across a series of
837 wavelengths (800-1250 nm; 10 nm interval) in both channels simultaneously (10 frames per
838 wavelength; saved as a time averaged projection). The laser attenuation was calibrated to maintain
839 constant power at the sample across the spectra, adjusting for wavelength-dependent laser output
840 and attenuation variance. Laser power and PMT gains were calibrated to prevent saturation of
841 PMTs at peak excitation values (XCaMP-Y: 970nm, RCatchER: 1100 nm), while ensuring
842 sufficient signal could be observed at 1010 nm. We recorded pre- and post-recording power
843 measurements and calibration frames to verify that power did not attenuate over the course of the
844 experiment, photobleaching did not occur and there was no degradation of the photodiodes. For
845 processing, we concatenated the image series using FIJI and performed ROI detection and transient
846 extraction using Suite2P. We background subtracted the traces (including removing
847 autofluorescence contamination, likely due to the older age of the mouse used), normalized these
848 to maximum power and performed a cubic interpolation between the discrete emission values to
849 produce the spectra curves.
850
851 **REFERENCES**
852

853 1.   Mekahli, D., Bultynck, G., Parys, J., De Smedt, H. & Missiaen, L. Endoplasmic-
854 Reticulum Calcium Depletion and Disease. *Cold Spring Harbor Perspectives in Biology* **3**
855 (2011).
856 2.   Verkhratsky, A. & Shmigol, A. Calcium-induced calcium release in neurones. *Cell*
857 *Calcium* **19**, 1-14 (1996).
858 3.   Ghosh, A. & Greenberg, M.E. Calcium signaling in neurons - molecular mechanisms and
859 cellular consequences. *Science* **268**, 239-247 (1995).
860 4.   Berridge, M. Neuronal calcium signaling. *Neuron* **21**, 13-26 (1998).
861 5.   Reddish, F., Miller, C., Gorkhali, R. & Yang, J. Calcium Dynamics Mediated by the
862 Endoplasmic/Sarcoplasmic Reticulum and Related Diseases. *International Journal of Molecular*
863 *Sciences* **18** (2017).
864 6.   Suzuki, J., Kanemaru, K. & Iino, M. Genetically Encoded Fluorescent Indicators for
865 Organellar Calcium Imaging. *Biophysical Journal* **111**, 1119-1131 (2016).
866 7.   Dreier, J.P. & Reiffurth, C. The Stroke-Migraine Depolarization Continuum. *Neuron* **86**,
867 902-922 (2015).
868 8.   Leao, A.A.P. Spreading depression of activity in the cerebral cortex. *Journal of*
869 *Neurophysiology* **7**, 359-390 (1944).
870 9.   Somjen, G.G. Aristides Leao's discovery of cortical spreading depression. *Journal of*
871 *Neurophysiology* **94**, 2-4 (2005).
872 10.   Leao, A.A.P. Further Observations on the Spreading Depression of Activity in the
873 Cerebral Cortex. *Journal of Neurophysiology* **10**, 409-414 (1947).
874 11.   Hills, K.E., Kostarelos, K. & Wykes, R.C. Converging Mechanisms of Epileptogenesis
875 and Their Insight in Glioblastoma. *Frontiers in Molecular Neuroscience* **15**, 23 (2022).

12. Dohmen, C.*, et al.* Spreading depolarizations occur in human ischemic stroke with high incidence. *Annals of Neurology* **63**, 720-728 (2008).

13. Lauritzen, M.*, et al.* Clinical relevance of cortical spreading depression in neurological disorders: migraine, malignant stroke, subarachnoid and intracranial hemorrhage, and traumatic brain injury. *Journal of Cerebral Blood Flow and Metabolism* **31**, 17-35 (2011).

14. Strong, A.J.*, et al.* Spreading and synchronous depressions of cortical activity in acutely injured human brain. *Stroke* **33**, 2738-2743 (2002).

15. Curry, R.N.*, et al.* Glioma epileptiform activity and progression are driven by IGSF3-mediated potassium dysregulation. *Neuron* **111**, 682-+ (2023).

16. Kramer, D.R., Fujii, T., Ohiorhenuan, I. & Liu, C.Y. Interplay between Cortical Spreading Depolarization and Seizures. *Stereotactic and Functional Neurosurgery* **95**, 1-5 (2017).

17. Tamim, I.*, et al.* Spreading depression as an innate antiseizure mechanism. *Nature Communications* **12**, 1-15 (2021).

18. Calia, A.B.*, et al.* Full-bandwidth electrophysiology of seizures and epileptiform activity enabled by flexible graphene microtransistor depth neural probes. *Nature Nanotechnology* **17**, 301-309 (2022).

19. Aiba, I., Ning, Y. & Noebels, J.L. A hyperthermic seizure unleashes a surge of spreading depolarizations in Scn1a-deficient mice. *Jci Insight* **8**, 19 (2023).

20. Koroleva, V.I., Vinogradova, L.V. & Bures, J. Reduced incidence of cortical spreading depression in the course of pentylenetetrazol kindling in rats. *Brain Research* **608**, 107-114 (1993).

21. Dreier, J.P.*, et al.* Spreading convulsions, spreading depolarization and epileptogenesis in human cerebral cortex. *Brain* **135**, 259-275 (2012).

22. Fabricius, M.*, et al.* Association of seizures with cortical spreading depression and peri-infarct depolarisations in the acutely injured human brain. *Clinical Neurophysiology* **119**, 1973-1984 (2008).

23. Raimondo, J.V., Burman, R.J., Katz, A.A. & Akerman, C.J. Ion dynamics during seizures. *Frontiers in Cellular Neuroscience* **9**, 14 (2015).

24. Traynelis, S.F. & Dingledine, R. Role of Extracellular-Space in Hyperosmotic Suppression of Potassium-Induced Electrographic Seizures. *Journal of Neurophysiology* **61**, 927-938 (1989).

25. McBain, C.J., Traynelis, S.F. & Dingledine, R. Regional Variation of Extracellular-Space in the Hippocampus. *Science* **249**, 674-677 (1990).

26. Somjen, G.G. *Ions in the Brain: Normal Function, Seizures, and Stroke* (Oxford University Press, New York, 2004).

27. Aiba, I. & Noebels, J.L. Spreading depolarization in the brainstem mediates sudden cardiorespiratory arrest in mouse SUDEP models. *Science Translational Medicine* **7**, 9 (2015).

28. Stern, M.A., Cole, E.R., Gross, R.E. & Berglund, K. Seizure event detection using intravital two-photon calcium imaging data. *Neurophotonics* **11**, 024202 (2024).

29. Basarsky, T.A., Duffy, S.N., Andrew, R.D. & MacVicar, B.A. Imaging spreading depression and associated intracellular calcium waves in brain slices. *Journal of Neuroscience* **18**, 7189-7199 (1998).

30. Nedergaard, M., Cooper, A.J.L. & Goldman, S.A. Gap-Junctions are Required for the Propagation of Spreading Depression. *Journal of Neurobiology* **28**, 433-444 (1995).

921   31.   Enger, R*., et al.* Dynamics of Ionic Shifts in Cortical Spreading Depression. *Cerebral*
922   *Cortex* **25**, 4469-4476 (2015).
923   32.   Lado, F.A. & Moshé, S.L. How do seizures stop? *Epilepsia* **49**, 1651-1664 (2008).
924   33.   Inoue, M*., et al.* Rational Engineering of XCaMPs, a Multicolor GECI Suite for In Vivo
925   Imaging of Complex Brain Circuit Dynamics. *Cell* **177**, 1346-1360 (2019).
926   34.   Deng, X.N*., et al.* Tuning Protein Dynamics to Sense Rapid Endoplasmic-Reticulum
927   Calcium Dynamics. *Angewandte Chemie-International Edition* **60**, 23289-23298 (2021).
928   35.   André, V., Pineau, N., Motte, J.E., Marescaux, C. & Nehlig, A. Mapping of neuronal
929   networks underlying generalized seizures induced by increasing doses of pentylenetetrazol in the
930   immature and adult rat:: a c-Fos immunohistochemical study. *European Journal of Neuroscience*
931   **10**, 2094-2106 (1998).
932   36.   Nathanson, J.L., Yanagawa, Y., Obata, K. & Callaway, E.M. Preferential labeling of
933   inhibitory and excitatory cortical neurons by endogenous tropism of adeno-associated virus and
934   lentivirus vectors. *Neuroscience* **161**, 441-450 (2009).
935   37.   Liou, J.Y*., et al.* Multivariate regression methods for estimating velocity of ictal
936   discharges from human microelectrode recordings. *Journal of Neural Engineering* **14**, 11 (2017).
937   38.   Smith, E.H*., et al.* Human interictal epileptiform discharges are bidirectional traveling
938   waves echoing ictal discharges. *Elife* **11**, 20 (2022).
939   39.   Marshall, W.H. Spreading cortical depression of Leao. *Physiological Reviews* **39**, 239-
940   279 (1959).
941   40.   Heck, C.N*., et al.* Two-year seizure reduction in adults with medically intractable partial
942   onset epilepsy treated with responsive neurostimulation: Final results of the RNS System Pivotal
943   trial. *Epilepsia* **55**, 432-441 (2014).
944   41.   Geller, E.B*., et al.* Brain-responsive neurostimulation in patients with medically
945   intractable mesial temporal lobe epilepsy. *Epilepsia* **58**, 994-1004 (2017).
946   42.   Hogan, P.G., Lewis, R.S. & Rao, A. Molecular Basis of Calcium Signaling in
947   Lymphocytes: STIM and ORAI. in *Annual Review of Immunology, Vol 28* (ed. W.E. Paul, D.R.
948   Littman & W.M. Yokoyama) 491-533 (Annual Reviews, Palo Alto, 2010).
949   43.   Gilbert, G*., et al.* Calcium Signaling in Cardiomyocyte Function. *Cold Spring Harbor*
950   *Perspectives in Biology* **12**, 29 (2020).
951   44.   Akerboom, J*., et al.* Crystal Structures of the GCaMP Calcium Sensor Reveal the
952   Mechanism of Fluorescence Signal Change and Aid Rational Design. *Journal of Biological*
953   *Chemistry* **284**, 6455-6464 (2009).
954   45.   Ali, F. & Kwan, A.C. Interpreting in vivo calcium signals from neuronal cell bodies,
955   axons, and dendrites: a review. *Neurophotonics* **7**, 17 (2020).
956   46.   Kucharz, K. & Lauritzen, M. CaMKII-dependent endoplasmic reticulum fission by
957   whisker stimulation and during cortical spreading depolarization. *Brain* **141**, 1049-1062 (2018).
958   47.   Khoshkhoo, S., Vogt, D. & Sohal, V.S. Dynamic, Cell-Type-Specific Roles for
959   GABAergic Interneurons in a Mouse Model of Optogenetically Inducible Seizures. *Neuron* **93**,
960   291-298 (2017).
961   48.   Tran, C.H*., et al.* Interneuron Desynchronization Precedes Seizures in a Mouse Model of
962   Dravet Syndrome. *Journal of Neuroscience* **40**, 2764-2775 (2020).
963   49.   Farrell, J.S*., et al.* In vivo assessment of mechanisms underlying the neurovascular basis
964   of postictal amnesia. *Scientific Reports* **10**, 13 (2020).
965   50.   Heuser, K*., et al.* Ca2+ Signals in Astrocytes Facilitate Spread of Epileptiform Activity.
966   *Cerebral Cortex* **28**, 4036-4048 (2018).

51. Van Harreveld, A. & Stamm, J.S. Consequences of cortical convulsive activity in rabbit. *Journal of Neurophysiology* **17**, 505-520 (1954).

52. Van Harreveld, A. & Stamm, J.S. Cortical response to metrazol and sensory stimulation in the rabbit. *Electroencephalography and Clinical Neurophysiology* **7**, 363-370 (1955).

53. Vergnes, M. & Marescaux, C. Cortical and thalamic lesions in rats with genetic absence epilepsy. *Journal of Neural Transmission-General Section*, 71-83 (1992).

54. Vinogradova, L., Kuznetsova, G. & Coenen, A. Audiogenic seizures associated with a cortical spreading depression wave suppress spike-wave discharges in rats. *Physiology & Behavior* **86**, 554-558 (2005).

55. Somjen, G.G. Mechanisms of spreading depression and hypoxic spreading depression-like depolarization. *Physiological Reviews* **81**, 1065-1096 (2001).

56. Wei, Y., Ullah, G. & Schiff, S. Unification of Neuronal Spikes, Seizures, and Spreading Depression. *Journal of Neuroscience* **34**, 11733-11743 (2014).

57. Dietz, R.M., Weiss, J.H. & Shuttleworth, C.W. Zn2+ influx is critical for some forms of spreading depression in brain slices. *Journal of Neuroscience* **28**, 8014-8024 (2008).

58. Pal, S., Sombati, S., Limbrick, D.D. & DeLorenzo, R.J. In vitro status epilepticus causes sustained elevation of intracellular calcium levels in hippocampal neurons. *Brain Research* **851**, 20-31 (1999).

59. Sham, J.S.K., Cleemann, L. & Morad, M. Functional coupling of Ca2+ channels and ryanodine receptors in cardiac myocytes. *Proceedings of the National Academy of Sciences of the United States of America* **92**, 121-125 (1995).

60. Furuichi, T.*, et al.* Multiple types of ryanodine receptor Ca2+ release channels are differentially expressed in rabbit brain. *Journal of Neuroscience* **14**, 4794-4805 (1994).

61. Lanner, J.T., Georgiou, D.K., Joshi, A.D. & Hamilton, S.L. Ryanodine Receptors: Structure, Expression, Molecular Details, and Function in Calcium Release. *Cold Spring Harbor Perspectives in Biology* **2**, 21 (2010).

62. Copello, J.A., Barg, S., Onoue, H. & Fleischer, S. Heterogeneity of Ca2+ gating of skeletal muscle and cardiac ryanodine receptors. *Biophysical Journal* **73**, 141-156 (1997).

63. Fill, M. & Copello, J.A. Ryanodine receptor calcium release channels. *Physiological Reviews* **82**, 893-922 (2002).

64. Foskett, J.K., White, C., Cheung, K.H. & Mak, D.O.D. Inositol trisphosphate receptor Ca2+ release channels. *Physiological Reviews* **87**, 593-658 (2007).

65. Giorgi, C., Marchi, S. & Pinton, P. The machineries, regulation and cellular functions of mitochondrial calcium. *Nature Reviews Molecular Cell Biology* **19**, 713-730 (2018).

66. Zhang, S.Y.L.*, et al.* STIM1 is a Ca2+ sensor that activates CRAC channels and migrates from the Ca2+ store to the plasma membrane. *Nature* **437**, 902-905 (2005).

67. Park, C.Y.*, et al.* STIM1 Clusters and Activates CRAC Channels via Direct Binding of a Cytosolic Domain to Orai1. *Cell* **136**, 876-890 (2009).

68. Pietrobon, D. & Moskowitz, M.A. Chaos and commotion in the wake of cortical spreading depression and spreading depolarizations. *Nature Reviews Neuroscience* **15**, 379-393 (2014).

69. Aiba, I., Wehrens, X.H.T. & Noebels, J.L. Leaky RyR2 channels unleash a brainstem spreading depolarization mechanism of sudden cardiac death. *Proceedings of the National Academy of Sciences of the United States of America* **113**, E4895-E4903 (2016).

70. Wuytack, F., Raeymaekers, L. & Missiaen, L. Molecular physiology of the SERCA and SPCA pumps. *Cell Calcium* **32**, 279-305 (2002).

71.   Sato, S.S., *et al.* Simultaneous two-photon imaging of intracellular chloride concentration and pH in mouse pyramidal neurons in vivo. *Proceedings of the National Academy of Sciences of the United States of America* **114**, E8770-E8779 (2017).

72.   Sun, X.L., *et al.* Simultaneous monitoring of intracellular pH changes and hemodynamic response during cortical spreading depression by fluorescence-corrected multimodal optical imaging. *Neuroimage* **57**, 873-884 (2011).

73.   Menyhárt, A., *et al.* Age or ischemia uncouples the blood flow response, tissue acidosis, and direct current potential signature of spreading depolarization in the rat brain. *American Journal of Physiology-Heart and Circulatory Physiology* **313**, H328-H337 (2017).

74.   Menyhárt, A., *et al.* Spreading depolarization remarkably exacerbates ischemia-induced tissue acidosis in the young and aged rat brain. *Scientific Reports* **7**, 13 (2017).

75.   Kim, J.H., *et al.* Noninvasive measurement of the pH of the endoplasmic reticulum at rest and during calcium release. *Proceedings of the National Academy of Sciences of the United States of America* **95**, 2997-3002 (1998).

76.   Dreier, J.P., *et al.* Terminal spreading depolarization and electrical silence in death of human cerebral cortex. *Annals of Neurology* **83**, 295-310 (2018).

77.   Carlson, A.P., *et al.* Terminal spreading depolarizations causing electrocortical silencing prior to clinical brain death: case report. *Journal of Neurosurgery* **131**, 1773-1779 (2019).

78.   Hernandez-Caceres, J., Macias-Gonzalez, R., Brozek, G. & Bures, J. Systemic ketamine blocks cortical spreading depression but does not delay the onset of terminal anoxia depolarization in rats. *Brain Research* **437**, 360-364 (1987).

79.   Müller, M. & Somjen, G.G. Inhibition of major cationic inward currents prevents spreading depression-like hypoxic depolarization in rat hippocampal tissue slices. *Brain Research* **812**, 1-13 (1998).

80.   Collins, F., Schmidt, M.F., Guthrie, P.B. & Kater, S.B. Sustained increase in intracellular calcium promotes neuronal survival. *Journal of Neuroscience* **11**, 2582-2587 (1991).

81.   Franklin, J.L. & Johnson, E.M. Suppression of programmed neuronal death by sustained elevation of cytoplasmic calcium. *Trends in Neurosciences* **15**, 501-508 (1992).

82.   Heinemann, U. & Lux, H.D. Ceiling of stimulus induced rises in extracellular potassium concentration in the cerebral-cortex of cat. *Brain Research* **120**, 231-249 (1977).

83.   Anderson, D., *et al.* Closed-loop stimulation in periods with less epileptiform activity drives improved epilepsy outcomes. *Brain* **147**, 521-531 (2024).

84.   Huang, X.P., *et al.* AAV2 production with optimized N/P ratio and PEI-mediated transfection results in low toxicity and high titer for in vitro and in vivo applications. *J. Virol. Methods* **193**, 270-277 (2013).

85.   Goldey, G.J., *et al.* Removable cranial windows for long-term imaging in awake mice. *Nature Protocols* **9**, 2515-2538 (2014).

86.   Roome, C.J. & Kuhn, B. Chronic cranial window with access port for repeated cellular manipulations, drug application, and electrophysiology. *Frontiers in Cellular Neuroscience* **8**, 8 (2014).

87.   Roome, C.J. & Kuhn, B. Voltage Imaging with ANNINE Dyes and Two-Photon Microscopy. in *Multiphoton Microscopy* (ed. E. Hartveit) 297-334 (Humana Press Inc, Totowa, 2019).

88.   Moucka, R., Sedlacík, M., Osicka, J. & Pata, V. Mechanical properties of bulk Sylgard 184 and its extension with silicone oil. *Scientific Reports* **11**, 9 (2021).

89. Stern, M.A.*, et al.* Applications of Bioluminescence-Optogenetics in Rodent Models. *Methods Mol Biol* **2525**, 347-363 (2022).

90. Jiang, S.*, et al.* Automated, highly reproducible, wide-field, light-based cortical mapping method using a commercial stereo microscope and its applications. *Biomed. Opt. Express* **7**, 3478-3490 (2016).

91. Ferezou, I.*, et al.* Spatiotemporal dynamics of cortical sensorimotor integration in behaving mice. *Neuron* **56**, 907-923 (2007).

92. Mason, C.R. & Cooper, R.M. Permanent change in convulsive threshold in normal and brain-damaged rats with repeated small doses of pentylenetetrazol. *Epilepsia* **13**, 663-& (1972).

93. Schindelin, J.*, et al.* Fiji: an open-source platform for biological-image analysis. *Nature Methods* **9**, 676-682 (2012).

94. Pachitariu, M.*, et al.* Suite2p: beyond 10,000 neurons with standard two-photon microscopy. *bioRxiv*, 061507 (2017).

95. Stringer, C., Wang, T., Michaelos, M. & Pachitariu, M. Cellpose: a generalist algorithm for cellular segmentation. *Nature Methods* **18**, 100-106 (2021).

96. Wenzel, M., Hamm, J.P., Peterka, D.S. & Yuste, R. Reliable and Elastic Propagation of Cortical Seizures In Vivo. *Cell Reports* **19**, 2681-2693 (2017).

97. Somarowthu, A., Goff, K.M. & Goldberg, E.M. Two-photon calcium imaging of seizures in awake, head-fixed mice. *Cell Calcium* **96**, 8 (2021).

98. Rolston, J.D., Laxpati, N.G., Gutekunst, C.-A., Potter, S.M. & Gross, R.E. Spontaneous and evoked high-frequency oscillations in the tetanus toxin model of epilepsy. *Epilepsia* **51**, 2289-2296 (2010).

Author contributions:
Conceptualization: MAS, KB, REG; Methodology: MAS, KB; Software: MAS, ERC; Validation: MAS, KB, ERC; Formal analysis: MAS, ERC, KB; Investigation: MAS, KB, CAG; Resources: REG, KB, JJY, CAG, MAS; Data curation: MAS, ERC, KB; Writing—original draft: MAS; Writing—review and editing: MAS, KB, ERC, CAG, JJY, REG; Visualization: MAS, KB, ERC, CAG; Supervision: REG, KB; Project administration: MAS; Funding acquisition: REG, KB, MAS

Competing interests: JJY is the shareholder of InLighta Biosciences and is a named inventor on an issued patent (US10371708) for R-CatchER. REG has received research support and personal fees outside the submitted work from NeuroPace, Inc., owner of the RNS® system. The terms of these arrangement have been reviewed and approved by Emory University and Georgia State University, in accordance with their conflict-of-interest policies. All other authors declare they have no competing interests.

Data and materials availability: The viral vector plasmids generated from this project will be made available to researchers upon request through a material transfer agreement. All data needed

1104   to evaluate the conclusions in the paper are present in the paper and/or the Supplementary Material.

1105   Code and summary data needed to replicate figures in the paper are publicly archived at Zenodo

1106   [repository pending, will be updated prior to publication]. Updated versions of the code will be

1107   available at the GitHub repository: https://github.com/Stern-MA/RCatchER_CSD.